43363

National Library of Canada
Canadian Theses Division
Ottawa, Canada
K1A 0N4

Bibliothèque nationale du Canada
Division des thèses canadiennes

PERMISSION TO MICROFILM — AUTORISATION DE MICROFILMER

• Please print or type — Écrire en lettres moulées ou dactylographier

Full Name of Author — Nom complet de l'auteur

Harold Neale Cardinal

Date of Birth — Date de naissance
February 9, 1954

Country of Birth — Lieu de naissance
Canada

Permanent Address — Résidence fixe
232 Lawson Rd, Westhill Ontario, M1C 2J7

Title of Thesis — Titre de la thèse

Échelle Spectrograph Design for the University of Alberta 0.5 m Cassegrain Telescope

University — Université
University of Alberta

Degree for which thesis was presented — Grade pour lequel cette thèse fut présentée
MSc

Year this degree conferred — Année d'obtention de ce grade
1979

Name of Supervisor — Nom du directeur de thèse
Dr. Douglas P. Hube

Permission is hereby granted to the NATIONAL LIBRARY OF CANADA to microfilm this thesis and to lend or sell copies of the film.

The author reserves other publication rights, and neither the thesis nor extensive extracts from it may be printed or otherwise reproduced without the author's written permission.

L'autorisation est, par la présente, accordée à la BIBLIOTHÈQUE NATIONALE DU CANADA de microfilmer cette thèse et de prêter ou de vendre des exemplaires du film.

L'auteur se réserve les autres droits de publication; ni la thèse ni de longs extraits de celle-ci ne doivent être imprimés ou autrement reproduits sans l'autorisation écrite de l'auteur.

Date
October 18, 1979

Signature
H. Neale Cardinal

NL-91 (4/77)

National Library of Canada

Cataloguing Branch
Canadian Theses Division

Ottawa, Canada
K1A 0N4

Bibliothèque nationale du Canada

Direction du catalogage
Division des thèses canadiennes

NOTICE

The quality of this microfiche is heavily dependent upon the quality of the original thesis submitted for microfilming. Every effort has been made to ensure the highest quality of reproduction possible.

If pages are missing, contact the university which granted the degree.

Some pages may have indistinct print especially if the original pages were typed with a poor typewriter ribbon or if the university sent us a poor photocopy.

Previously copyrighted materials (journal articles, published tests, etc.) are not filmed.

Reproduction in full or in part of this film is governed by the Canadian Copyright Act, R.S.C. 1970, c. C-30. Please read the authorization forms which accompany this thesis.

THIS DISSERTATION
HAS BEEN MICROFILMED
EXACTLY AS RECEIVED

AVIS

La qualité de cette microfiche dépend grandement de la qualité de la thèse soumise au microfilmage. Nous avons tout fait pour assurer une qualité supérieure de reproduction.

S'il manque des pages, veuillez communiquer avec l'université qui a conféré le grade.

La qualité d'impression de certaines pages peut laisser à désirer, surtout si les pages originales ont été dactylographiées à l'aide d'un ruban usé ou si l'université nous a fait parvenir une photocopie de mauvaise qualité.

Les documents qui font déjà l'objet d'un droit d'auteur (articles de revue, examens publiés, etc.) ne sont pas microfilmés.

La reproduction, même partielle, de ce microfilm est soumise à la Loi canadienne sur le droit d'auteur, SRC 1970, c. C-30. Veuillez prendre connaissance des formules d'autorisation qui accompagnent cette thèse.

LA THÈSE A ÉTÉ
MICROFILMÉE TELLE QUE
NOUS L'AVONS REÇUE

THE UNIVERSITY OF ALBERTA

ÉCHELLE SPECTROGRAPH DESIGN FOR THE UNIVERSITY OF ALBERTA 0.5 m CASSEGRAIN TELESCOPE

by

© H. NEALE CARDINAL

A THESIS

SUBMITTED TO THE FACULTY OF GRADUATE STUDIES AND RESEARCH

IN PARTIAL FULFILLMENT OF THE REQUIREMENTS FOR THE DEGREE

OF MASTER OF SCIENCE

DEPARTMENT OF PHYSICS

EDMONTON, ALBERTA

FALL, 1979

THE UNIVERSITY OF ALBERTA

FACULTY OF GRADUATE STUDIES AND RESEARCH

The undersigned certify that they have read, and recommend to the Faculty of Graduate Studies and Research for acceptance, a thesis entitled "Échelle Spectrograph Design for the University of Alberta 0.5 m Cassegrain Telescope" submitted by H. Neale Cardinal in partial fulfillment of the requirements for the degree of Master of Science.

Supervisor

R. F. Egerton

J. S. Martin

E. Pimmington

Date: October 17, 1979

ABSTRACT

An échelle spectrograph is designed for the University of Alberta 0.5 m telescope, for use at the f/8 folded Cassegrain focus. The advantages of échelle spectrographs over conventional coudé instruments are described and the applicable scalar grating theory developed, including new expressions for the échelle order width and grating efficiency. Design considerations leading to the selection of the optimal Bausch and Lomb gratings to cover the spectral range 3400-8800 Å in two exposures are given, and the output format described. The spectrograph uses a magnetically focused single-stage ITT F-4089 image-tube and a thorium comparison source, and reaches an estimated $4^{m}.5$ in one hour on untreated IIa-D plates. A third-order design for an off-axis field-flattened Schmidt camera is executed, but optimization computations by Dr. Harvey E. Richardson of Dominion Astrophysical Observatory indicate large residual higher-order aberrations remain. An improved design using transmission cross-disperser gratings will be published in a future joint paper.

ACKNOWLEDGEMENTS

It is a great pleasure to thank here all those who have helped to make this thesis possible: Dr. Stanley Jeffers, of York University, for extensive information and advice; Dr. John Lester, of the University of Toronto, for many helpful suggestions, including using Thorium as a comparison source; Mr. Chris Morbey, of Dominion Astrophysical Observatory, for his informative discussion of the work done there with image-tubes; and most especially Dr. Harvey Richardson, also of Dominion Astrophysical Observatory, for many fruitful discussions and his inestimable aid in designing the spectrograph camera. Finally, I would also like to thank my supervisor, Dr. Douglas Hube, for his patience and guidance throughout the course of this work.

TABLE OF CONTENTS

		Page
	INTRODUCTION	
CHAPTER 1	ADVANTAGES OF ÉCHELLE SPECTROGRAPHS	4
CHAPTER 2	GRATING THEORY	6
	Energy Distribution of the Diffraction Pattern	6
	Blazed Wavelength	15
	Resolution and Dispersion	16
	Free Spectral Range and Order Separation	18
	Échelle Gratings	20
	Ends of Échelle Orders	21
	Grating Efficiency	31
CHAPTER 3	DESIGN EQUATIONS	35
	Elements of an Échelle Spectrograph	35
	Projected Slit Width and Resolution	36
	Throughput	38
	Plate Factor	39
	Spectral Line Tilt	40
	Order Separation	41
	Exit Pupil Considerations	42
CHAPTER 4	SPECTROGRAPH DESIGN	46
	Choice of Collimator	46
	Choice of Cross-Disperser	47

Page

CHAPTER 4 (Cont'd)

Orientation of Échelle 49

Selection of Échelle Groove Spacing and Blaze Angle 50

Selection of Cross-Disperser Groove Spacing and Blaze Wavelength 57

Optimizing the Blaze of Hα, Hβ, Hγ, Hδ and K Lines 59

Detailed Computation of the Final Design 61

CHAPTER 5 CAMERA DESIGN 75

Preliminary Design 78

Final Design 86

CHAPTER 6 DETECTOR SELECTION 89

Plate Selection 89

For Direct Exposures 92

For Image-Tube Exposures 92

Image-Tube Selection 93

CHAPTER 7 MISCELLANEA 99

Comparison Source Selection 99

Limiting Magnitude of the Spectrograph 100

Practical Considerations 103

Grating Ordering Information 104

REFERENCES 105

LIST OF TABLES

Table		Page
4.1	Bausch & Lomb échelles.	51
4.2	$m_{max}-m_{min}$ for the échelles shown in Table 4.1, corresponding to λ_{min} = 3400 Å, λ_{max} = 8800 Å.	53
4.3(a)	Approximate spectrograph parameters for an échelle-collimator separation of $(f_1-\ell')$.	55
4.3(b)	Approximate spectrograph parameters for an échelle-collimator separation of $(2f_1)$.	56
4.4	Effective order numbers, m_{eff}, for Hα, Hβ, Hγ, Hδ and K lines. The rms deviations from the (nearest) order numbers and the échelle efficiency $E(\beta_B)$ corresponding to each value of θ are also shown.	60
4.5	Échelle order characteristics for short wavelength range.	63,64
4.6	Échelle order characteristics for long wavelength range.	66,67
6.1	Characteristics of ITT F-4089 magnetically focused image tube, with an MA-3 photocathode and P-20 phosphor screen.	98

LIST OF FIGURES

Figure		Page
2.1	Grating parameters, shown for an échelle grating with $\alpha \geq \phi, \beta$.	7
2.2	Blaze efficiency of an ordinary grating for orders $m = 1,2,3$.	13
2.3	Échelle blaze efficiency.	14
3.1	Gaussian (first order) layout of Cassegrain telescope plus collimator.	45
4.1	Short wavelength range image.	65
4.2	Long wavelength range image.	68
4.3(a)	Side view of the spectrograph, drawn to one-half scale.	71
4.3(b)	Top view of the spectrograph, drawn to one-half scale.	72
5.1	Illumination pattern of camera corrector plate, drawn to full scale.	76
5.2	Sectioning of the plane mirror and the spherical mirror, drawn to one-quarter scale.	83
5.3	Preliminary camera design, drawn to one-quarter scale.	84
6.1	Approximate spectral sensitivities of Kodak spectroscopic plates, for a one-hour exposure.	91
6.2	Spectral energy distribution of P-11 and P-20 phosphor screens.	91

INTRODUCTION

The purpose of this thesis is to present, in detail, a design for a high-dispersion spectrograph for use at the f/8 Cassegrain focus of the University of Alberta's 20-inch (0.508 m) telescope, located at the Devon Observatory, about 16 miles (26 km) southwest of Edmonton.

The telescope is fork mounted, with the f/3 paraboloidal primary mounted in an octagonal aluminum cradle, to which three interchangeable upper tubes can be attached, to produce a prime focus and f/8 or f/18 classical Cassegrain foci. An 18-inch (0.457 m) aperture Baker reflector-corrector has been designed for the prime focus, while two aspheric plates and a field flattener will allow wide-field work at the f/8 focus, and a simple field-flattening lens will correct the rather strong field curvature at the f/18 focus.

In normal use, however, the telescope is set up in the f/8 configuration, with the correcting lenses replaced by an indexing diagonal, near the primary, which directs the converging beam to one of six observation ports around the cradle. This arrangement allows the spectrograph to be permanently mounted at the side of the cradle without interfering with other uses of the telescope. A photometer, for use at the f/18 focus, will similarly occupy another port.

Due to the restricted space available, the spectrograph must be less than about 0.2 m (8 inches) wide, 0.3 m

(12 inches) high, and roughly 1 m (3 feet) long. Also, it should not be so heavy as to cause overloading, balancing or flexure problems on the telescope, or handling difficulties in case it should ever need to be removed. An upper limit of 30 kg (66 lbs) meets these requirements. (This figure is somewhat arbitrary, but it is the luggage limit on most airlines.)

Due to the requirements of high dispersion and resolution, spectrograph designs employing a series of prisms as the dispersing element are generally unsuitable, as well as suffering from heavy absorption at shorter wavelengths. The choice then remains between conventional grating spectrographs, employing a plane or concave grating, with a high groove density, in low order, or échelle spectrographs, which use a coarse grating in high orders of interference.

Since échelle gratings are of necessity used at high angles of incidence, the precision required to successfully rule échelle gratings is an order of magnitude greater than for conventional gratings, and such gratings have become generally available only in the last decade or so. For this reason, much of the theory of échelle gratings presented in this thesis is new, and is therefore developed in detail.

Although the recent advent of holographically ruled gratings allows the use of much higher groove densities (and hence higher dispersion and resolution

for a given collimator size in a given order) than otherwise feasible, and these gratings offer greatly reduced scattered light over conventional rulings, the sinusoidal and near-sinusoidal groove shapes which result reduce their efficiencies to about 1/3 to 1/4 that of échellette (stair-shaped) gratings. Thus, since the exposure times required to produce a suitably dense spectrum must be kept relatively short, we will only consider using conventionally ruled gratings. (We remark that there are no holographic échelle gratings.).

In order to decrease the exposure time of an object of given magnitude, or, equivalently, to increase the limiting magnitude of the spectrograph for a given exposure, we will design our spectrograph for use with an image-tube. Since such tubes are very costly, it may be financially desirable to first construct the spectrograph, and then add the image-tube at a later date. An image-tube is a practical necessity, however, for a spectrograph operating on a medium sized telescope such as the 0.5 m, since otherwise the light grasp of the instrument would be insufficient to effectively study most objects of astrophysical interest.

With these considerations in mind, we now investigate the reasons for choosing as the design for our intrument that of an échelle spectrograph.

CHAPTER 1

ADVANTAGES OF ÉCHELLE SPECTROGRAPHS

As stated by Schroeder (1970), a spectrograph employing an échelle grating as the principal dispersing element enjoys several advantages over a conventional grating instrument.

The primary advantage is in size. Because an échelle has much higher angular dispersion than a conventional grating, compact spectrographs suitable for medium sized Cassegrain telescopes can be designed which give plate factors of a few Ångströms per millimeter, normally obtainable only with large coudé spectrographs (of conventional design).

The second advantage is in resolution and/or throughput. For a given telescope, the product of the spectrograph resolution and throughput is proportional to the collimator diameter and angular dispersion. The advantage of the échelle can easily be a factor of three or more.

The third advantage is a two-dimensional output format, particularly suited to image-tubes. A secondary dispersing element is used to separate the échelle orders from each other, perpendicular to the main échelle dispersion, so that the resulting spectrum is a series of ~ 100 Å segments, stacked one on top of another. Thus, typically 2000-3000 Å of spectrum can be recorded in a single

image-tube exposure, as opposed to the single ~ 100 Å strip covered by a coudé spectrograph of comparable dispersion. The decreased efficiency caused by the introduction of this cross-disperser is amply offset by the elimination of the extra mirrors required to reach the coudé focus with a conventional grating spectrograph.

As expected, there is a price to be paid for all these advantages. The variation of the échelle efficiency across each order, and the variation of cross-disperser efficiency and, more importantly, image-tube gain over the large wavelength range covered by a single exposure, complicate the problem of fixing background intensities in stellar spectra. Also, the angular dispersion varies by several percent across each order, requiring careful wavelength determinations using more comparison lines. However, these disadvantages in ease of calibration are of minor consequence compared to the advantages listed above.

In the next two chapters, we develope the necessary background for the preceding statements, and lay the foundations for the design calculations which follow.

CHAPTER 2

GRATING THEORY

Energy Distribution of the Diffraction Pattern

We now examine the energy distribution of the diffraction pattern of a plane grating in the scalar approximation. This approximation consists of assigning the light waves an amplitude and phase only, ignoring their polarization. According to Loewen (1977), efficiency measurements show progressively greater difference between the diffracted intensity of light polarized parallel (p-plane) or perpendicular (s-plane) to the grating grooves as the ratio of wavelength to groove spacing, λ/d, increases. For $\lambda/d < 0.2$, polarization effects are negligible, while they become noticeable for $\lambda/d > 0.4$. By a fortunate circumstance, there is a partial compensation between the two planes, so that the averaged output, or efficiency in unpolarized light, is given to good approximation by the scalar theory for $\lambda/d < 0.4$. For our present purpose, therefore, it will turn out that scalar theory is perfectly adequate to describe grating behavior.

The various grating parameters are defined in Figure 2.1, which shows the side and top views of a typical échelle grating. An ordinary plane grating would differ only in having a smaller blaze angle, ϕ, and thus would be oriented more nearly normal to the incident beam.

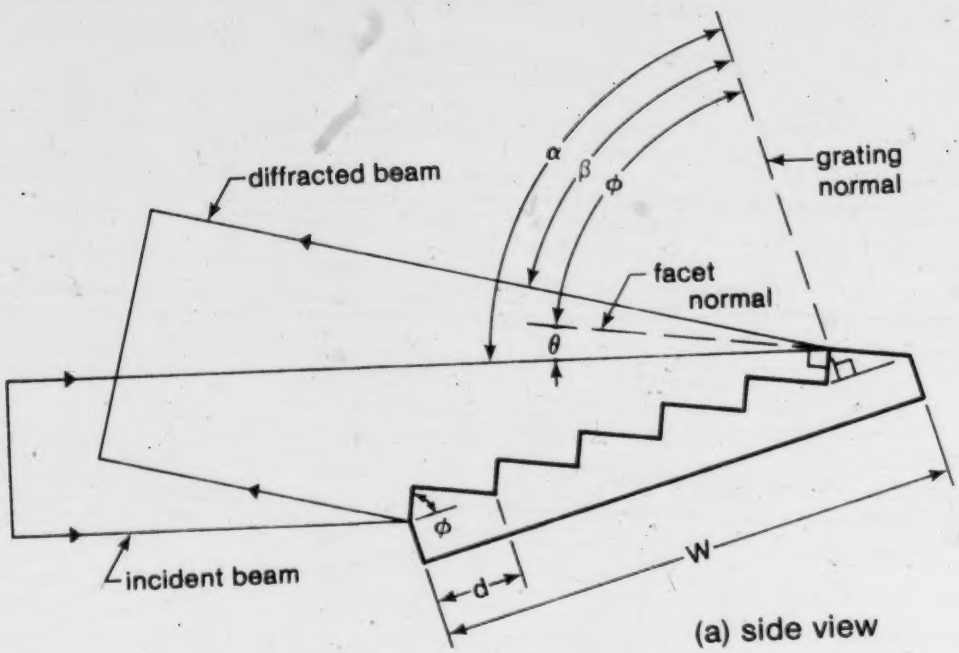

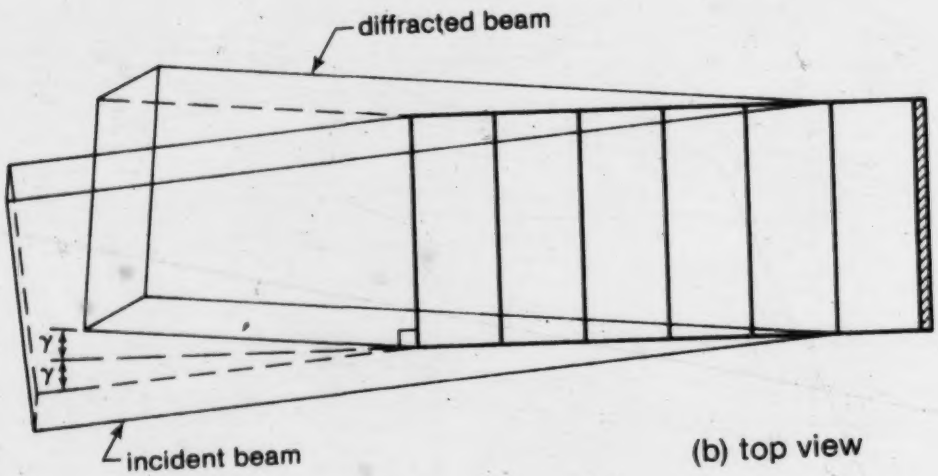

α angle of incidence
β angle of diffraction
γ skew angle

$\theta = |\alpha - \phi|$
ϕ blaze angle

d groove spacing
$N = d^{-1}$ grating constant
W grating width

Figure 2.1: Grating parameters, shown for an échelle grating with $\alpha \geq \phi, \beta$. By convention, angles are positive on the same side of the grating normal as the facet normal, so that $\phi > 0$.

We have assumed $\alpha \geq \phi, \beta$ in Figure 2.1 since this is the normal orientation of échelles. By convention, α and β are positive when measured on the same side of the grating normal as the facet normal.

The path difference between two rays of light diffracted by successive grooves is, by simple geometry

$$\Delta = d \cos \gamma (\sin \alpha + \sin \beta) \quad . \tag{2.1}$$

For constructive interference, this path difference must be an integral number of wavelengths, i.e. $\Delta = m\lambda$ or

$$m\lambda = d \cos \gamma (\sin \alpha + \sin \beta) \tag{2.2}$$

where m is the order number. Equation 2.2 is called the grating equation. The phase difference between the waves diffracted by two consecutive grooves is

$$\delta \equiv \frac{2\pi\Delta}{\lambda} = \frac{2\pi d}{\lambda} \cos \gamma (\sin \alpha + \sin \beta) \quad . \tag{2.3}$$

Hence, if the grating has K grooves and the elementary waves all have the same aplitude A_o, then the total amplitude is

$$A = \sum_{k=1}^{K} A_o e^{-ik\delta} = A_o \frac{\sin(\frac{K\delta}{2})}{\sin(\frac{\delta}{2})} \tag{2.4}$$

and since $Kd = W$, the diffracted intensity $I(\beta) = |A|^2$ or

$$I(\beta) = |A_o|^2 \frac{\sin^2[\frac{\pi W}{\lambda} \cos \gamma (\sin \alpha + \sin \beta)]}{\sin^2[\frac{\pi d}{\lambda} \cos \gamma (\sin \alpha + \sin \beta)]} \tag{2.5}$$

which has principal maxima at $\frac{d}{\lambda} \cos \gamma(\sin\alpha + \sin \beta) = m$, m an integer, and we recover the grating equation. Up to this point our treatment is exact. Now, in the scalar approximation, each groove is effectively a single slit of width

$$d' = d \cos \phi(1 - \tan(\chi - \phi) \tan \phi), \quad \chi = \max(\alpha, \beta, \phi) \qquad 2.6$$

by simple geometry. Hence each elementary wave is described by the single slit diffraction pattern†

$$|A_o|^2 = I_o \operatorname{sinc}^2(\tfrac{1}{2} \delta') \qquad 2.7$$

where $\operatorname{sinc} x \equiv \frac{\sin x}{x}$ and δ' is the phase difference between the two edges of the slit, found from simple geometry to be (cf. equation 2.3)

$$\delta' = \frac{2\pi d'}{\lambda} \cos \gamma(\sin(\alpha - \phi) + \sin(\beta - \phi)) \ . \qquad 2.8$$

Hence, we find the diffracted intensity distribution

$$I(\beta) = B(\beta)\, I_o \frac{\sin^2[\frac{\pi W}{\lambda} \cos \gamma(\sin\alpha + \sin \beta)]}{\sin^2[\frac{\pi d}{\lambda} \cos \gamma(\sin\alpha + \sin \beta)]} \qquad 2.9$$

where $B(\beta)$ is the blaze efficiency function, given in the scalar approximation by

$$B(\beta) = \operatorname{sinc}^2[\frac{\pi d'}{\lambda} \cos \gamma(\sin(\alpha - \phi) + \sin(\beta - \phi))]. \qquad 2.10$$

---

† See, e.g., Waves - Berkeley Physics Course Volume 3, p. 485.

Gray (1976) gives a more rigorous derivation of equation 2.10, which is his equation 3-10, although still in the scalar approximation; however, he incorrectly sets $d' = d$. Schroeder (1970) gives d' correctly for the case $\alpha \geq \phi, \beta$.

Now $B(\beta)$ has its principal maximum when $\sin(\alpha - \phi) + \sin(\beta - \phi) = 0$, i.e. in the direction of the blazed β, β_B, defined by

$$\alpha + \beta_B = 2\phi \qquad 2.11$$

i.e.

$$\alpha = \phi \pm \theta , \quad \beta_B = \phi \mp \theta \qquad 2.12$$

with the signs chosen according to whether α is greater or less than ϕ. We remark that equation 2.11 is just the condition for specular reflection from the groove facets. Using the grating equation 2.2 to substitute for λ[†] and the definition of β_B, we can rewrite equation 2.10 for $B(\beta)$ as follows:

$$B(\beta) = \operatorname{sinc}^2\left[\frac{m\pi d'}{d}\left(\frac{\sin(\alpha-\phi) + \sin(\beta-\phi)}{\sin\alpha + \sin\beta}\right)\right]$$

$$= \operatorname{sinc}^2\left[\frac{m\pi d'}{d}\left(\cos\phi - \sin\phi\left(\frac{\cos\alpha + \cos\beta}{\sin\alpha + \sin\beta}\right)\right)\right]$$

$$= \operatorname{sinc}^2\left[\frac{m\pi d' \cos\phi}{d}\left(1 + \frac{\tan\phi}{\tan\frac{1}{2}(\alpha+\beta)}\right)\right]$$

[†]Note that this substitution is not valid for $m = 0$, where $\beta = -\alpha$ for all wavelengths.

$$= \text{sinc}^2\left[\frac{m\pi d' \cos\phi}{d}\left(1 - \frac{\tan\phi}{\tan(\phi + \frac{1}{2}(\beta - \beta_B))}\right)\right]$$

$$= \text{sinc}^2\left[\frac{m\pi d'}{d\cos\phi}\left(\frac{\tan\frac{1}{2}(\beta - \beta_B)}{\tan\phi + \tan\frac{1}{2}(\beta - \beta_B)}\right)\right] \quad . \qquad 2.13$$

Substituting for d' from equation 2.6, we are led to three cases:

$$B_o(\beta) = \text{sinc}^2\left[\frac{m\pi \tan\frac{1}{2}(\beta - \beta_B)}{\tan\phi + \tan\frac{1}{2}(\beta - \beta_B)}\right] \qquad \phi \geq \alpha,\beta \qquad 2.14$$

$$B_1(\beta) = \text{sinc}^2\left[\frac{m\pi \tan\frac{1}{2}(\beta - \beta_B)}{\tan\phi + \tan\frac{1}{2}(\beta - \beta_B)}(1 - \tan\theta\tan\phi)\right] \qquad 2.15$$

$$\alpha \geq \phi,\beta$$

$$B_2(\beta) = \text{sinc}^2\left[\frac{m\pi \tan\frac{1}{2}(\beta - \beta_B)}{\tan\phi + \tan\frac{1}{2}(\beta - \beta_B)}(1 - \tan(\beta-\phi)\tan\phi)\right] \qquad 2.16$$

$$\beta \geq \phi,\alpha$$

We remark that for the case $\beta_B = \phi + \theta$, we have the geometric identity

$$1 - \tan(\beta - \phi)\tan\phi = 1 - \tan(\theta + \beta - \beta_B)\tan\phi$$

$$= (1 - \tan\theta\tan\phi)\left(\frac{1 - \tan\beta_B \tan(\beta - \beta_B)}{1 - \tan\theta\tan(\beta - \beta_B)}\right)$$

2.17

For the remainder of this section, we will restrict our attention to the case $\alpha \geq \phi,\beta$ described by equation 2.15. In this case $\alpha = \phi + \theta$, $\beta_B = \phi - \theta$.

For ordinary gratings θ and ϕ are both small so we may write $B_1(\beta) \simeq B_o(\beta)$. This is equivalent to neglecting the non-illuminated portion of the grooves. Since $B_o(\beta)$ is a function only of $\tan\frac{1}{2}(\beta-\beta_B)/\tan\phi$, we can plot a universal blaze function, shown in Figure 2.2 for orders $m = 1,2,3$. Since $\text{sinc}^2(0.443\,\pi) = \frac{1}{2}$, blaze efficiency exceeds 50% for

$$-\frac{0.443}{m+0.443} < \frac{\tan\frac{1}{2}(\beta-\beta_B)}{\tan\phi} < \frac{0.443}{m-0.443} \qquad 2.18$$

and similarly exceeds 75% for

$$-\frac{0.292}{m+0.292} < \frac{\tan\frac{1}{2}(\beta-\beta_B)}{\tan\phi} < \frac{0.292}{m-0.292}\,. \qquad 2.19$$

For échelle gratings, $\tan\phi > 1 >> \tan\frac{1}{2}(\beta-\beta_B)$. Hence, using the trivial approximation $\tan\frac{1}{2}(\beta-\beta_B) \approx \frac{1}{2}(\beta-\beta_B)$, which we neglect relative to $\tan\phi$, we have

$$B_1(\beta) \simeq \text{sinc}^2\left[\frac{\pi}{2}\left(\frac{1-\tan\theta\tan\phi}{\tan\phi}\right) m(\beta-\beta_B)\right] \equiv B_E(\beta). \qquad 2.20$$

Since the echelle blaze function $B_E(\beta)$ is a function only of $m(\beta-\beta_B)$, we can again plot a universal curve, valid for $m \gtrsim 10$. This is shown in Figure 2.3 for the cases $\phi = 63.435°$ $(\tan\phi = 2)$ and $\theta = 0°, 7°$.

To estimate the error in using these approximations, we first note that

$$\frac{d}{dx}(\text{sinc}^2 x) = -2\left(1-\frac{x}{\tan x}\right)\frac{\text{sinc}^2 x}{x}\,. \qquad 2.21$$

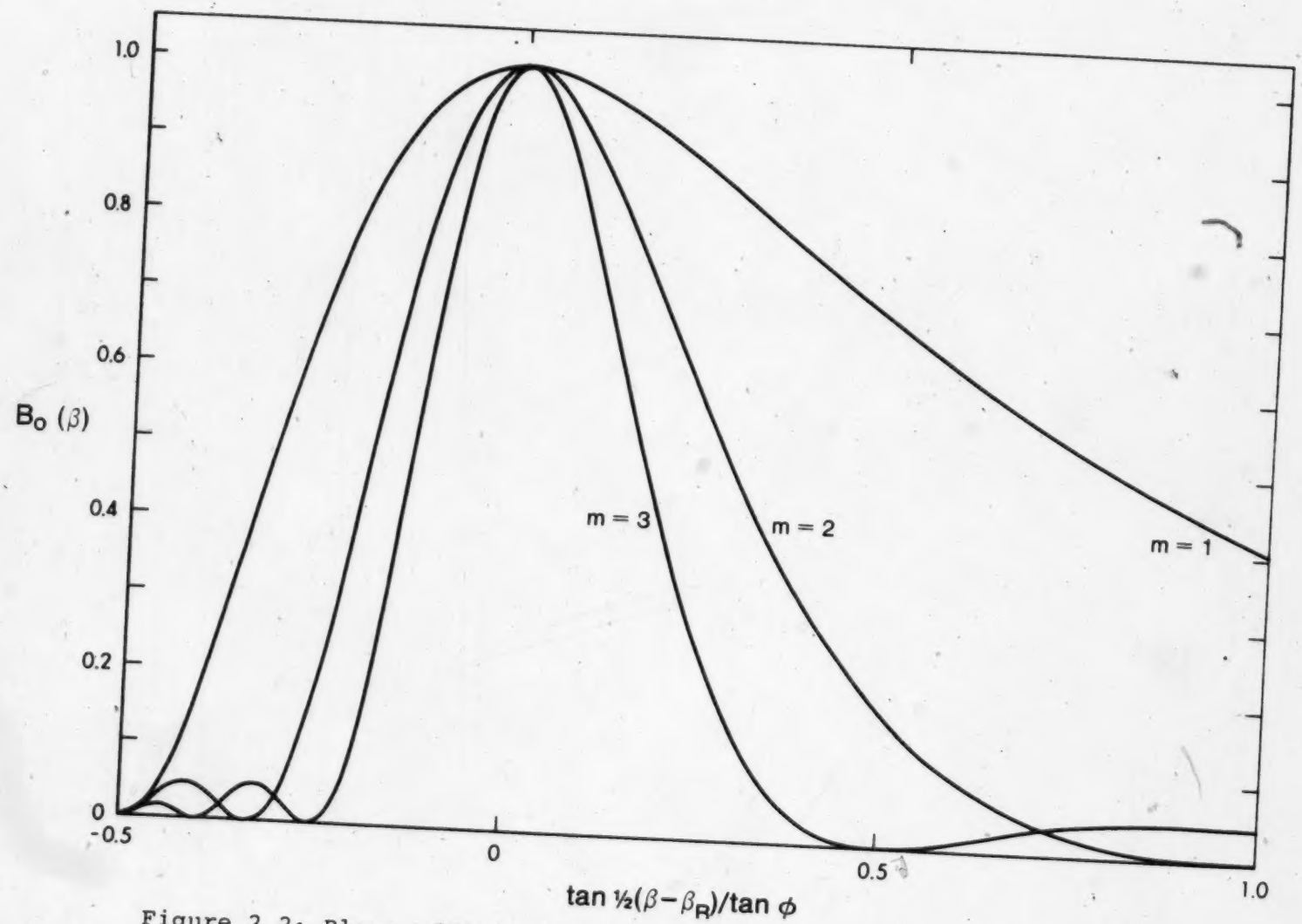

Figure 2.2: Blaze efficiency of an ordinary grating for orders m = 1,2,3.

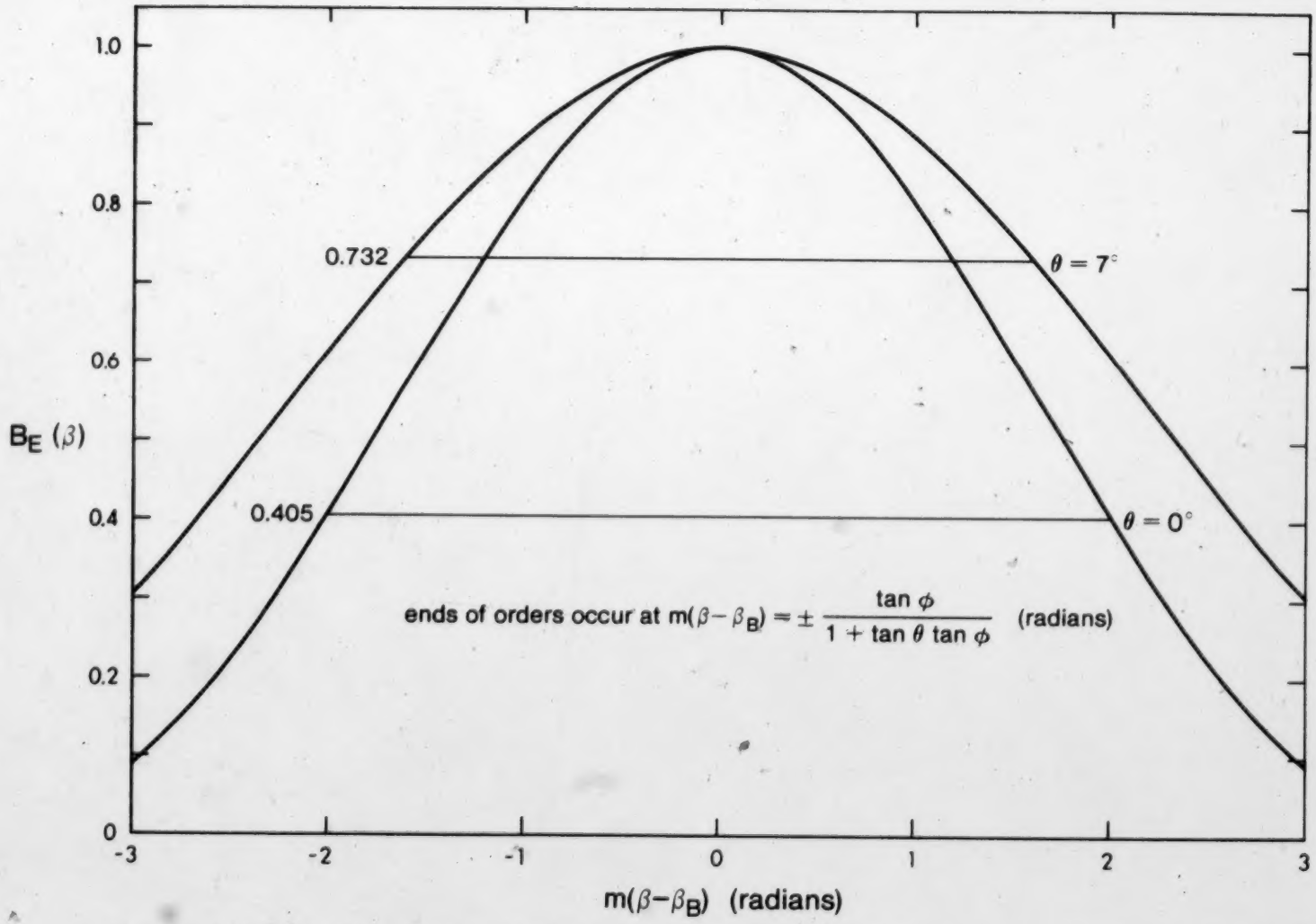

Figure 2.3: Échelle blaze efficiency. Curves shown are for $\phi = 63.435°$, $(\tan\phi = 2)$.

Hence the error in $\text{sinc}^2 x$ due to an error δx in x is approximately

$$\delta \text{sinc}^2 x \simeq 2\left(1 - \frac{x}{\tan x}\right) \text{sinc}^2 x \left(\frac{\delta x}{x}\right) < 0.84\left(\frac{\delta x}{x}\right). \quad 2.22$$

Thus the absolute differences of the approximate blaze functions from $B_1(\beta)$ are bounded as follows:

$$\delta B_o(\beta) < 0.84 \tan\theta \tan\phi \quad 2.23$$

$$\delta B_E(\beta) < 0.42 |\beta - \beta_B| / \tan\phi \quad . \quad 2.24$$

At the end of this chapter, we will show that, within the $B_E(\beta)$ approximation, the ends of the échelle orders occur at

$$m(\beta - \beta_B) = \pm \frac{\tan\phi}{1 + \tan\theta \tan\phi} \quad . \quad 2.25$$

Hence, within the échelle orders, we have

$$\delta B_E(\beta) < 0.42 \frac{|\beta - \beta_B|}{\tan\phi} \leq \frac{0.42}{m(1 + \tan\theta \tan\phi)} \quad . \quad 2.26$$

Of course, similar approximations can be made for the other cases, but they will not be needed for the design calculations and are, therefore, omitted.

Blazed Wavelength

The wavelength λ_B, corresponding to the direction β_B in order m is easily found from the grating equation 2.2 and equation 2.12 to be

$$\lambda_{B'} = \frac{d \cos\gamma(\sin\alpha + \sin\beta_B)}{m} = \frac{2d \cos\gamma \sin\phi \cos\theta}{m} . \quad 2.27$$

However, by convention, for ordinary gratings, the blazed wavelength λ_B is always given for Littrow configuration ($\gamma = \theta = 0$) in first order ($m = 1$):

$$\lambda_B = 2d \sin\phi \quad . \quad 2.28$$

Thus, for ordinary gratings, N (grooves/mm) and λ_B are usually specified instead of d and ϕ. We remark that the effective blazed wavelength $\lambda_{B'}$ is always shorter than λ_B, viz:

$$\lambda_{B'} = \cos\gamma \cos\theta \, \lambda_B/m \quad . \quad 2.29$$

Of course, échelle gratings are not intended for first order use and are therefore described by N and ϕ (or tan ϕ, which is always chosen to be an integer). As we shall see, the échelle orders have considerable overlap, and thus an échelle can be considered to be effectively blazed for all wavelengths.

Resolution and Dispersion

From equation 2.5 or 2.9, the first zero of the diffracted intensity distribution differs from the central maximum by an amount

$$d(\cos\gamma(\sin\alpha + \sin\beta)) = \lambda/W \quad . \quad 2.30$$

For fixed α and γ, this becomes

$$d\beta = \frac{\lambda}{W \cos\gamma \cos\bar{\beta}} = \left(\frac{\sin\alpha + \sin\beta}{\cos\bar{\beta}}\right) \frac{d}{mW} \quad . \qquad 2.31$$

Thus $d\beta$ represents the angular resolution of the grating by the Rayleigh criterion, which states that two diffraction patterns are just resolved if the central maximum of one falls on the first zero of the other.

If we differentiate the grating equation 2.2 with respect to wavelength, we find, for fixed α and γ, that the angular dispersion is

$$\frac{d\beta}{d\lambda} = \frac{m}{d \cos\gamma \cos\beta} = \left(\frac{\sin\alpha + \sin\beta}{\cos\beta}\right) \frac{1}{\lambda} \quad . \qquad 2.32$$

Hence the angular dispersion depends only on the working angular conditions. On the blaze peak, $\beta = \beta_B$, we can use equation 2.12 to write

$$\frac{d\beta}{d\lambda} = \left(\frac{2 \tan\phi}{1 \pm \tan\theta \tan\phi}\right) \frac{1}{\lambda} \simeq \frac{2 \tan\phi}{\lambda} \qquad 2.33$$

where the last expression is valid for small θ. Thus, other things being equal, the angular dispersion is (approximately) proportional to $\tan\phi$. For this reason, échelle gratings, with $\tan\phi = 2$ or even $\tan\phi = 4$ enjoy much greater dispersive power than ordinary gratings, which have blaze angles ϕ of only a few to several degrees.

The minimum resolvable wavelength difference $d\lambda$ is found by inserting the angular resolution $d\beta$ given by

equation 2.31 into the dispersion formula 2.32. The result is usually quoted in the form of the theoretical resolution, R_o, defined by

$$R_o \equiv \frac{\lambda}{d\lambda} = \frac{mW}{d} = \cos\gamma(\sin\alpha + \sin\beta)\frac{W}{\lambda} \quad . \qquad 2.34$$

Of course, grating imperfections will detract from this number slightly, but, in practice, the achievable resolution of a spectrograph is almost always limited by the finite width of the entrance slit, as we shall see in the next chapter.

Free Spectral Range and Order Separation

From the grating equation 2.2 it is obvious that many wavelengths are dispersed at the same angle of diffraction β. In adjacent orders m_1 and $m_2 = m_1 + 1$, we therefore have

$$m_1\lambda_1 = m_2\lambda_2 = d\cos\gamma(\sin\alpha + \sin\beta) \quad . \qquad 2.35$$

Hence the free spectral range $\Delta\lambda = \lambda_1 - \lambda_2$ is given by

$$\Delta\lambda = d\cos\gamma(\sin\alpha + \sin\beta)\left(\frac{1}{m_1} - \frac{1}{m_2}\right)$$

$$= \frac{d\cos\gamma(\sin\alpha + \sin\beta)}{m_1 m_2} = \frac{\lambda_1\lambda_2}{d\cos\gamma(\sin\alpha + \sin\beta)}$$

$$= \lambda_1/m_2 = \lambda_2/m_1 \quad . \qquad 2.36$$

Thus, wavelengths in the range $\lambda_2 < \lambda < \lambda_1$ can be observed in order m_1 with no overlap from other orders. Hence, to avoid contamination of the spectrum, wavelengths outside

the free spectral range must be suppressed or separated from those in the order of interest.

For a grating used in first order, $\Delta\lambda = \frac{1}{2}\lambda_1$, and the spectral coverage over some range of diffraction angle is:

$$m = 2: \quad \frac{1}{4}\lambda_1 - \frac{1}{2}\lambda_1$$

$$m = 1: \quad \boxed{\frac{1}{2}\lambda_1 - \lambda_1} \quad . \qquad 2.37$$

Hence, a cutoff filter may be used to eliminate wavelengths shorter than $\frac{1}{2}\lambda_1$ from the spectrum. Glass filters with a sharp cutoff, selectable to within 200 Å, are easily available for wavelengths covering most of the visible and near ultraviolet spectrum.

If the grating is used in second order, however, the situation is more complex. The free spectral range is now $\Delta\lambda = \frac{1}{3}\lambda_1$, and the spectral coverage, over a now narrower range of diffraction angles, is:

$$m = 3: \quad \frac{4}{3}\lambda_1 - \frac{2}{3}\lambda_1$$

$$m = 2: \quad \boxed{\frac{2}{3}\lambda_1 - \lambda_1}$$

$$m = 1: \quad \frac{4}{3}\lambda_1 - 2\lambda_1 \quad . \qquad 2.38$$

Thus wavelengths shorter than $\frac{2}{3}\lambda_1$ and longer than $\frac{4}{3}\lambda_1$ must be eliminated. However, the availability of a suitable cuton filter to perform this latter task is doubtful.

Copper sulphate between glass and other liquid filters must usually be resorted to, entailing many practical difficulties, not the least of which is the risk of freezing!

For échelle gratings, which are used in high orders of interference, we can approximate the free spectral range in order m as

$$\Delta\lambda \approx \frac{d \cos\gamma(\sin\alpha + \sin\beta)}{m^2} = \frac{\lambda^2}{d\cos\gamma(\sin\alpha+\sin\beta)} = \frac{\lambda}{m} \qquad 2.39$$

which becomes impractically small for the use of filters, and a different approach is used.

Échelle Gratings

Échelle gratings are coarse (10-100 gr/mm) gratings used in high orders of interference (m = 10-100). They have steep blaze angles ($\tan\phi = 2,4$) for high angular dispersion. Due to their small free spectral ranges, an auxiliary disperser, with its direction of dispersion perpendicular to that of the échelle, is used to separate the orders. This results in a two-dimensional 'stacked' or 'raster' format of the spectrum, which is particularly suited to the coverage of large spectral regions (2000-3000 Å) at high dispersion (a few Å/mm) on small detectors, such as image-tubes.

Ends of Échelle Orders

We will consider the ends of two adjacent échelle orders to be at that wavelength where the blaze efficiencies coincide. Spectral lines still appear in an order outside this 'end', but with a lower intensity than in the next order. At an 'end wavelength', most of the light is divided evenly between the two orders, in contrast to a blazed wavelength, which is concentrated largely in a single order. We remark that since $m \geq 10$ for échelle gratings, we have

$$\lambda/d = \cos\gamma(\sin\alpha + \sin\beta)/m < 2/m \leq 0.2 \qquad 2.40$$

and thus polarization effects are always negligible, and the échelle blaze efficiency is well described by the scalar theory developed earlier.

For the remainder of this section, we will restrict our attention to the case $\alpha \geq \phi, \beta$ described by equation 2.15. In this case $\alpha = \phi + \theta$, $\beta_B = \phi - \theta$.

Suppose now that échelle order m_1 ends at $\beta = \beta_1$ and order $m_2 = m_1 + 1$ ends at $\beta = \beta_2$, then we must have

$$\frac{m_1 \tan\frac{1}{2}(\beta_1 - \beta_B)}{\tan\phi + \tan\frac{1}{2}(\beta_1 - \beta_B)} = -\frac{m_2 \tan\frac{1}{2}(\beta_2 - \beta_B)}{\tan\phi + \tan\frac{1}{2}(\beta_2 - \beta_B)} = -c \qquad 2.41$$

or

$$\frac{\tan\frac{1}{2}(\beta_1 - \beta_B)}{\tan\phi} = -\frac{c}{m_1 + c} \qquad 2.42$$

$$\frac{\tan\frac{1}{2}(\beta_2 - \beta_B)}{\tan\phi} = \frac{c}{m_2 - c} \qquad 2.43$$

Also, since the échelle orders both end at some wavelength λ^*, we have also, from the grating equation 2.2, that

$$\sin \beta_1 = \frac{m_1 \lambda^*}{d \cos \gamma} - \sin \alpha \qquad 2.44$$

$$\sin \beta_2 = \frac{m_2 \lambda^*}{d \cos \gamma} - \sin \alpha \quad . \qquad 2.45$$

Since $\tan \frac{1}{2}(\beta - \beta_B) = \frac{\sin \beta - \sin \beta_B}{\cos \beta + \cos \beta_B}$, the last four equations combine to give

$$\frac{m_1 \lambda^*}{d \cos \gamma \tan \phi} - \frac{\sin \alpha + \sin \beta_B}{\tan \phi} = -\frac{c}{m_1 + c} (\cos \beta_1 + \cos \beta_B) \qquad 2.46$$

$$\frac{m_2 \lambda^*}{d \cos \gamma \tan \phi} - \frac{\sin \alpha + \sin \beta_B}{\tan \phi} = \frac{c}{m_2 - c} (\cos \beta_2 + \cos \beta_B) \qquad 2.47$$

Since $\mathrm{sinc}^2 [\pi c(1 - \tan \theta \tan \phi)] > 0$, $c \leq 1$. Hence let $c = \frac{1}{2} + c'$. Then, if $\bar{m} = \frac{1}{2}(m_1 + m_2) = m_1 + \frac{1}{2} = m_2 - \frac{1}{2}$, eliminating the wavelength λ^* from equations 2.46 and 2.47 yields

$$\frac{\sin \alpha + \sin \beta_B}{c \tan \phi} = \left(\frac{\bar{m} + \frac{1}{2}}{\bar{m} + c'}\right)(\cos \beta_1 + \cos \beta_B) + \left(\frac{\bar{m} - \frac{1}{2}}{\bar{m} - c'}\right)(\cos \beta_2 + \cos \beta_B). \qquad 2.48$$

From equations 2.42 and 2.43, $\tan \frac{1}{2}(\beta_1 - \beta_B) = 0(\frac{1}{\bar{m}})$, $\tan \frac{1}{2}(\beta_2 - \beta_B) = 0(\frac{1}{\bar{m}})$ and

$$\frac{\tan \frac{1}{2}(\beta_1 - \beta_B)}{\tan \frac{1}{2}(\beta_2 - \beta_B)} = -\left(\frac{\bar{m} - c'}{\bar{m} + c'}\right) = -1 + 0(\frac{1}{\bar{m}}) \quad . \qquad 2.49$$

Hence we can write

$$\beta_1 - \beta_B = -\beta' \qquad 2.50$$

$$\beta_2 - \beta_B = \beta' + \beta'' \qquad 2.51$$

where $\beta' = 0(\frac{1}{\bar{m}})$ and $\beta'' = 0(\frac{1}{\bar{m}^2})$. Then, within $0(\frac{1}{\bar{m}^2})$

$$\cos\beta_1 = \cos\beta_B \cos\beta' + \sin\beta_B \sin\beta' = \cos\beta_B + \beta' \sin\beta_B \qquad 2.52$$

$$\cos\beta_2 = \cos\beta_B \cos\beta' - \sin\beta_B \sin\beta' = \cos\beta_B - \beta' \sin\beta_B \qquad 2.53$$

Hence, within $0(\frac{1}{\bar{m}^2})$

$$\frac{\sin\alpha + \sin\beta_B}{c \tan\phi} = \left(\frac{\bar{m} + \frac{1}{2}}{\bar{m} + c'}\right)(2\cos\beta_B + \beta' \sin\beta_B) + \left(\frac{\bar{m} - \frac{1}{2}}{\bar{m} - c'}\right)(2\cos\beta_B - \beta' \sin\beta_B)$$

$$= \left(\frac{2\bar{m}^2 - c'}{\bar{m}^2 - c'^2}\right) 2\cos\beta_B + \left(\frac{1 - 2c'}{\bar{m}^2 - c'^2}\right) 2\bar{m}\,\beta' \sin\beta_B$$

$$= 4\cos\beta_B \qquad 2.54$$

Hence, since $\alpha = \phi + \theta$, $\beta = \phi - \theta$, we have, within $0(\frac{1}{\bar{m}^2})$:

$$c = \frac{1}{4\tan\phi}\left(\frac{\sin\alpha + \sin\beta_B}{\cos\beta_B}\right) = \frac{1}{2(1 + \tan\theta \tan\phi)} \qquad 2.55$$

$$c' = -\frac{\tan\theta}{4}\left(\frac{\sin\alpha + \sin\beta_B}{\cos\beta_B}\right) = \frac{-\tan\theta \tan\phi}{2(1 + \tan\theta \tan\phi)}\,. \qquad 2.56$$

Substituting these results into equations 2.42 and 2.43, we find, within $0(\frac{1}{\bar{m}^3})$:

$$\beta' = -2\tan\tfrac{1}{2}(\beta_1 - \beta_B) = \frac{2\tan\phi c}{\bar{m}+c'} = \frac{2\tan\phi c}{\bar{m}}\left(1-\frac{c'}{\bar{m}}\right)$$

$$= \Delta\beta + \tfrac{1}{2}\tan\theta(\Delta\beta)^2 \qquad 2.57$$

$$\beta' + \beta'' = 2\tan\tfrac{1}{2}(\beta_2 - \beta_B) = \frac{2\tan\phi c}{\bar{m}-c'} = \frac{2\tan\phi c}{\bar{m}}\left(1+\frac{c'}{\bar{m}}\right)$$

$$= \Delta\beta - \tfrac{1}{2}\tan\theta(\Delta\beta)^2 \qquad 2.58$$

where

$$\Delta\beta \equiv \frac{\tan\phi}{\bar{m}(1+\tan\theta\tan\phi)} = \frac{\sin\alpha+\sin\beta_B}{2\bar{m}\cos\beta_B} \quad . \qquad 2.59$$

Thus, if β^* denotes the angle of diffraction at the end of order $m = \bar{m} \pm \frac{1}{2}$, then, within $0(\frac{1}{\bar{m}^3})$:

$$\beta^* = \beta_B \pm \Delta\beta - \tfrac{1}{2}\tan\theta(\Delta\beta)^2 \quad . \qquad 2.60$$

Combining the result 2.55 with the definition 2.41 of c, we find from equation 2.15 that the value of the blaze function at the ends of the échelle orders is

$$B_1(\beta^*) = \mathrm{sinc}^2\left[\tfrac{\pi}{2}\left(\frac{1-\tan\theta\tan\phi}{1+\tan\theta\tan\phi}\right)\right] = \mathrm{sinc}^2\left[\tfrac{\pi}{2}\left(\frac{\cos\alpha}{\cos\beta_B}\right)\right] . \qquad 2.61$$

To find the ends of the orders in the $B_1(\beta) \simeq B_E(\beta)$ approximation, we require

$$B_E(\beta_E^*) \equiv \mathrm{sinc}^2\left[\tfrac{\pi}{2}\left(\frac{1-\tan\theta\tan\phi}{\tan\phi}\right) m(\beta_E^* - \beta_B)\right] = B_1(\beta^*) \qquad 2.62$$

which leads to the result

$$\beta_E^* = \beta_B \pm \Delta\beta_E \qquad 2.63$$

where

$$\Delta\beta_E = \frac{\tan\phi}{m(1+\tan\theta\tan\phi)} = \frac{\sin\alpha + \sin\beta_B}{2m\cos\beta_B} \qquad 2.64$$

as stated earlier in equation 2.25. We may also use this result to reformulate the definition 2.20 of $B_E(\beta)$ to read

$$B_E(\beta) = \mathrm{sinc}^2\left[\frac{\pi}{2}\left(\frac{\cos\alpha}{\cos\beta_B}\right)\frac{\beta-\beta_B}{\Delta\beta_E}\right] . \qquad 2.65$$

From the grating equation 2.2, the wavelength at the end of an order is simply

$$\lambda^* = d\cos\gamma(\sin\alpha + \sin\beta^*)/m . \qquad 2.66$$

From the dispersion relation 2.32, an error $\delta\beta^*$ in β^* gives rise to a relative wavelength error

$$\frac{\delta\lambda^*}{\lambda^*} \simeq \left(\frac{\cos\beta^*}{\sin\alpha+\sin\beta^*}\right)\delta\beta^* \simeq \left(\frac{\cos\beta_B}{\sin\alpha+\sin\beta_B}\right)\delta\beta^* = \frac{\delta\beta^*}{2m\Delta\beta_E} . \qquad 2.67$$

Comparing the expressions for $\Delta\beta$ and $\Delta\beta_E$, we find the error in β_E^* to be

$$\delta\beta_E^* = \Delta\beta_E/2m \qquad 2.68$$

corresponding to a wavelength error

$$\delta\lambda_E^* = \lambda_E^*/4m^2 \qquad 2.69$$

We now determine the next order term in the expansion 2.60 of β^*, which will lead us to an improved

determination of β^* (and hence λ^*), an estimate of the error $\delta\beta^*$ (and hence $\delta\lambda^*$), and, via equation 2.15, an estimate of the error $\delta B_1(\beta^*)$ in expression 2.61 for $B_1(\beta^*)$.

From the grating equation 2.2 (or equations 2.44 and 2.45) we can write

$$\frac{(\bar{m}+\frac{1}{2})\lambda^*}{(\bar{m}-\frac{1}{2})\lambda^*} = \frac{\sin\alpha + \sin\beta_2}{\sin\alpha + \sin\beta_1} \qquad 2.70$$

where, from equation 2.60,

$$\beta_2 = \beta_B + \Delta\beta - \frac{1}{2}\tan\theta\,(\Delta\beta)^2 + a(\Delta\beta)^3 \qquad 2.71$$

$$\beta_1 = \beta_B - \Delta\beta - \frac{1}{2}\tan\theta\,(\Delta\beta)^2 + b(\Delta\beta)^3 \qquad 2.72$$

hence

$$\sin\alpha = \bar{m}(\sin\beta_2 - \sin\beta_1) - \tfrac{1}{2}(\sin\beta_2 + \sin\beta_1)$$

$$= 2\bar{m}\cos\tfrac{1}{2}(\beta_2+\beta_1)\sin\tfrac{1}{2}(\beta_2-\beta_1) - \sin\tfrac{1}{2}(\beta_2+\beta_1)\cos\tfrac{1}{2}(\beta_2-\beta_1) \qquad 2.73$$

Substituting for β_1 and β_2 and using the expansions $\sin x = x - \frac{1}{6}x^3 + \ldots$ and $\cos x = 1 - \frac{1}{2}x^2 + \ldots$, we have, retaining terms to third order in $\Delta\beta$:

$$\sin\alpha = 2\bar{m}\Delta\beta\{\cos\beta_B + \sin\beta_B \cdot \tfrac{1}{2}(\tan\theta - (a+b)\Delta\beta)(\Delta\beta)^2\}$$
$$\times\{1 + \tfrac{1}{2}(a-b-\tfrac{1}{3})(\Delta\beta)^2\} - \{\sin\beta_B - \cos\beta_B \cdot \tfrac{1}{2}(\tan\theta - (a+b)\Delta\beta)(\Delta\beta)^2\}$$
$$\times\{1 - \tfrac{1}{2}(\Delta\beta)^2\} \quad . \qquad 2.74$$

From equation 2.59, $2\bar{m}\Delta\beta = (\sin\alpha + \sin\beta_B)/\cos\beta_B$, and the constant terms cancel. The choice $a + b = 0$ annuls the coefficient of $(\Delta\beta)^3$, and that of $(\Delta\beta)^2$ will then vanish, and equation 2.74 will be satisfied within $0(\Delta\beta)^4$, provided

$$0 = \left(\frac{\sin\alpha + \sin\beta_B}{\cos\beta_B}\right)\left(a - b - \frac{1}{3} + \tan\theta\tan\beta_B\right) + (\tan\theta + \tan\beta_B). \qquad 2.75$$

But, since $\alpha = \beta_B + 2\theta$, we have the trigonometric identity

$$\frac{\sin\alpha + \sin\beta_B}{\cos\beta_B} = \frac{\sin\beta_B(1+\cos 2\theta) + \cos\beta_B \sin 2\theta}{\cos\beta_B}$$

$$= \tan\beta_B\, 2\cos^2\theta + 2\sin\theta\cos\theta$$

$$= \frac{2(\tan\theta + \tan\beta_B)}{1 + \tan^2\theta} \qquad 2.76$$

which leads to the result:

$$b = -a = \frac{1}{12} + \frac{1}{2}\tan\theta\tan\beta_B + \frac{1}{4}\tan^2\theta \ . \qquad 2.77$$

Since the first two terms in 2.77 are generally comparable, while the third is much smaller, we write, for $m = \bar{m} \pm \frac{1}{2}$

$$\beta^* = \beta_B \pm \Delta\beta - \frac{1}{2}\tan\theta(\Delta\beta)^2 \mp \left(\frac{1}{12} + \frac{1}{2}\tan\theta\tan\beta_B\right)(\Delta\beta)^3 \qquad 2.78$$

with an error

$$\delta\beta^* = \frac{1}{4}\tan^2\theta(\Delta\beta)^3 \qquad 2.79$$

From equations 2.59 and 2.67, the relative wavelength error corresponding to the angular error $\delta\beta^*$ is

$$\frac{\delta\lambda^*}{\lambda^*} = \left(\frac{1 + \tan\theta \tan\phi}{\tan\phi}\right) \frac{\delta\beta^*}{2} \leq \left(\frac{1 + \tan\theta \tan\phi}{\tan\phi - \tan\theta}\right) \frac{\delta\beta^*}{2} = \frac{\delta\beta^*}{2 \tan\beta_B} \qquad 2.80$$

or, explicitly,

$$\frac{\delta\lambda^*}{\lambda^*} = \frac{\tan^2\theta}{8 \tan\beta_B} (\Delta\beta)^3 \quad . \qquad 2.81$$

We remark that replacing $m = \bar{m} + \frac{1}{2}$ by $m' = \bar{m} - \frac{1}{2}$ is equivalent, in formula 2.78, to replacing $\Delta\beta$ by $\Delta\beta' = -\Delta\beta$ (i.e. $\bar{m}$ by $-\bar{m}$), so that only a single polynomial need be evaluated, e.g. by a programmable calculator, to compute β^* for all orders of interest. Also, the magnitude of the actual errors can be checked by comparing the values of λ^* obtained for $m = \bar{m} \pm \frac{1}{2}$, which will differ by approximately $2\delta\lambda^*$. As a numerical example, we consider the case $\phi = 63.435°$ ($\tan\phi = 2$), $\theta = 7°$, for two different gratings:

For $N = 79$ grooves/mm, $\gamma = 0$, $\bar{m} = 25.5$, $\lambda^* = 8804.855$ Å, we obtain

$$\delta\beta^* \simeq 1 \times 10^{-6} \simeq 5 \times 10^{-5} \text{ degree} \simeq 0.2\text{" arc} \qquad 2.82$$

$$\delta\lambda^* \simeq 3 \times 10^{-7} \lambda^* \simeq 0.003 \text{ Å} \qquad 2.83$$

while the computed values of λ^* are 8804.852 Å ($m = 25$) and 8804.857 Å ($m = 26$), which differ by 0.005 Å, in agreement with the comments above.

For $N = 316$ grooves/mm, $\gamma = 0$, $\bar{m} = 5.5$, $\lambda^* = 10{,}003.0$ Å, we obtain

$$\delta\beta^* \simeq 1 \times 10^{-4} \simeq 5 \times 10^{-3} \text{ degree} \simeq 20'' \text{ arc} \qquad 2.84$$

$$\delta\lambda^* \simeq 2 \times 10^{-5}\,\lambda^* \simeq 0.3 \text{ Å} \qquad 2.85$$

but here the computed values of λ^* are 10,002.97 Å ($m = 5$) and 10,003.01 Å ($m = 6$) which means that the actual error is much less than that indicated by 2.84 and 2.85.

Thus it seems plausible that the actual error in equation 2.78 is bounded, for a given ϕ and θ. The maximum error in the above case probably lies somewhere between the two sets of figures shown, i.e. the maximum angular error $\delta\beta^*$ is a few seconds of arc. Since this approaches the resolution limit of most spectrograph cameras, further refinement of the theory here would seem pointless. We also remark that the full accuracy of any of the equations presented so far may only be obtained when ϕ and θ are precisely known, and in practice this will usually present the limiting factor on the accuracy of the computations, especially for wavelengths.

We now use equation 2.15 with the result 2.77 to compute $B_1(\beta^*)$ within $0(\Delta\beta)^3$. Since $\tan\frac{1}{2}x = \frac{1}{2}x + \frac{1}{24}x^3 + \ldots$, we have that for $m = \bar{m} \pm \frac{1}{2}$, within $0(\Delta\beta)^4$:

$$\tan\tfrac{1}{2}(\beta^* - \beta_B) = \pm\tfrac{1}{2}\Delta\beta - \tfrac{1}{4}\tan\theta\,(\Delta\beta)^2 \mp \tfrac{1}{8}\tan\theta\,(2\tan\beta_B + \tan\theta)(\Delta\beta)^3 \qquad 2.86$$

Substituting into equation 2.15, we find, using the definition 2.59 of $\Delta\beta$, that, within $0(\Delta\beta)^3$:

$$B_1(\beta^*) = \operatorname{sinc}^2\left\{\frac{\pi(\bar{m}\pm\frac{1}{2})\frac{\tan\phi(1-\tan\theta\tan\phi)}{2\bar{m}(1+\tan\theta\tan\phi)}\left(1\mp\frac{\tan\theta\tan\phi}{2\bar{m}(1+\tan\theta\tan\phi)}-\frac{\tan\theta\tan^2\phi(2\tan\beta_B+\tan\theta)}{4\bar{m}^2(1+\tan\theta\tan\phi)^2}\right)}{\tan\phi\pm\frac{\tan\phi}{2\bar{m}(1+\tan\theta\tan\phi)}\left(1\mp\frac{\tan\theta\tan\phi}{2\bar{m}(1+\tan\theta\tan\phi)}-\frac{\tan\theta\tan^2\phi(2\tan\beta_B+\tan\theta)}{4\bar{m}^2(1+\tan\theta\tan\phi)^2}\right)}\right\}$$

$$= \operatorname{sinc}^2\left\{\frac{\pi}{2}\left(\frac{1-\tan\theta\tan\phi}{1+\tan\theta\tan\phi}\right)\left\{\frac{1\pm\frac{1}{2\bar{m}(1+\tan\theta\tan\phi)}-\frac{\tan\theta\tan\phi(1+2\tan\phi(\tan\beta_B+\tan\theta))}{4\bar{m}^2(1+\tan\theta\tan\phi)^2}}{1\pm\frac{1}{2\bar{m}(1+\tan\theta\tan\phi)}-\frac{\tan\theta\tan\phi}{4\bar{m}^2(1+\tan\theta\tan\phi)^2}}\right\}\right\}$$

$$= \operatorname{sinc}^2\left\{\frac{\pi}{2}\left(\frac{1-\tan\theta\tan\phi}{1+\tan\theta\tan\phi}\right)\left(1-\frac{(\tan\theta\tan\beta_B+\tan^2\theta)\tan^2\phi}{2\bar{m}^2(1+\tan\theta\tan\phi)^2}\right)\right\}$$

$$= \operatorname{sinc}^2\left\{\frac{\pi}{2}\left(\frac{\cos\alpha}{\cos\beta_B}\right)\left(1-\frac{1}{2}\tan\theta(\tan\beta_B+\tan\theta)(\Delta\beta)^2\right)\right\} \qquad 2.87$$

Hence, since $(\tan\beta_B + \tan\theta) \leq \tan\phi$, we see from equation 2.22 that the error in expression 2.61 for $B_1(\beta^*)$ is

$$\delta B_1(\beta^*) < 0.42 \tan\theta \tan\phi (\Delta\beta)^2 . \qquad 2.88$$

For the case $\phi = 63.435°$, $\theta = 7°$, this becomes

$$\delta B_1(\beta^*) < 0.27/\bar{m}^2 \qquad 2.89$$

or $\delta B_1(\beta^*) < 0.0004$ for $\bar{m} = 25\frac{1}{2}$. Thus, although for $\theta > 0$ the blaze efficiency at the ends of the échelle orders is not a

true constant (since then, by equation 2.87, it depends on $\Delta\beta$ and hence $\bar{m}$), it is very nearly so, and the error in equation 2.61 is completely negligible.

Having now thoroughly explored the behavior of the blaze efficiency function in terms of the grating parameters, we now consider its significance in terms of grating performance.

Grating Efficiency

By definition, the absolute efficiency of a grating at a given wavelength is the energy diffracted into the order of interest relative to the incident energy. The efficiency, on the other hand, is the diffracted energy relative to the energy reflected from a mirror,coated identically to the grating, working under the same angular conditions. Within the scalar approximation, the absolute efficiency is just the efficiency times the reflectance τ of the grating coating.

From the considerations leading to equation 2.6 for the effective facet width, d', it can be seen that the factor $\tan(\chi-\phi)\tan\phi$, $\chi = \max(\alpha,\beta,\phi)$, describes the non-illuminated portion of the facets when $\alpha \geq \phi,\beta$, but represents the proportion of the incident light lost from the beam when $\beta > \alpha$ or $\phi > \alpha$. This is called shadowing of the grooves by Gray (1976), who remarks that aside from being lost from the beam, this light may also increase the level of scattered light in the spectrograph.

Thus, for the remainder of this section, we will again restrict our attention to the case $\alpha \geq \phi, \beta$, where there is no shadowing. Again, in this case $\alpha = \phi + \theta$, $\beta_B = \phi - \theta$.

Since energy equals intensity times beam size (area), and the factor I_o in equation 2.9 clearly includes the inverse beam size, it can be seen from this same equation that when the grating equation 2.2 is satisfied, the diffracted energy is proportional to the blaze efficiency function $B_1(\beta)$. Hence, since $B_1(\beta_B) = 1$, the efficiency is

$$E(\beta) = E(\beta_B) B_1(\beta) \quad . \qquad 2.90$$

This is confirmed by Figure 3-13 in Gray (1976). From the figures given by Loewen, Nevière and Maystre (1977), it can be further seen that $E(\beta_B) = 1$ in the Littrow configuration (i.e. $\theta = 0$; from equations 2.15 and 2.87 the value of γ does not influence the grating efficiency), and a blazed wavelength then appears only in a single order.

As θ increases from zero, the blaze distribution for each order flattens, while the efficiency of the blaze peak, $E(\beta_B)$, decreases from unity in such a way that the average efficiency across each order remains essentially constant. The blaze function flattens due to energy formerly concentrated near the peak of an échelle order now being diffracted into the wings of adjacent orders. For a uniform continuous spectrum, the same total energy would be distributed among essentially the same number of

orders, hence the energy per order and thus the average efficiency across each order must remain essentially constant.

Using the échelle blaze function $B_E(\beta)$, as given by equation 2.65, for simplicity, we thus have the condition that, for some constant k,

$$k = \frac{E(\beta_B)}{\Delta\beta_E} \int B_E(\beta)\, d\beta = E(\beta_B) \int_{-\infty}^{\infty} \operatorname{sinc}^2 \left[\frac{\pi}{2}\left(\frac{\cos\alpha}{\cos\beta_B}\right) \frac{\beta-\beta_B}{\Delta\beta_E}\right] d\left(\frac{\beta-\beta_B}{\Delta\beta_E}\right) . \qquad 2.91$$

We have extended the limits of integration to $\pm\infty$ since the integrand is small for $|\beta-\beta_B| \gtrsim 2\Delta\beta_E = 0(\frac{1}{m})$. Also $B_E(\beta)$ is closely equal to the even part of $B_1(\beta)$ about β_B for $|\beta-\beta_B| \lesssim 2\Delta\beta_E$, and $2\Delta\beta_E$ closely approximates the actual échelle order width. Hence the errors introduced by using this approximation are negligible. Now, for $a > 0$,

$$\int_{-\infty}^{\infty} \operatorname{sinc}^2(ax)\, dx = \frac{\pi}{a} . \qquad 2.92$$

Hence, with the choice $k = 2$ for correct normalization, equation 2.91 reduces to

$$E(\beta_B) = \frac{\cos\alpha}{\cos\beta_B} = \frac{1 - \tan\theta \tan\phi}{1 + \tan\theta \tan\phi} \qquad 2.93$$

and the theoretical efficiency is therefore approximately

$$E(\beta) = \frac{\cos\alpha}{\cos\beta_B} B_1(\beta) . \qquad 2.94$$

Although, in practice, grating imperfections lead to

efficiencies of from 70-90% of the theoretical efficiency, we will use equation 2.94 as an (optimistic) estimate of grating efficiency when calculating the spectrograph throughput.

In the next chapter we will use the grating equation blaze function, and the expressions derived from them for angular dispersion, échelle order width and grating efficiency, to derive the equations necessary to design an échelle spectrograph.

CHAPTER 3

DESIGN EQUATIONS

A spectrograph essentially converts the telescopic image of a star into one of its spectrum, which is then recorded photographically. To increase the sensitivity of the instrument, an image-tube is often used to intensify the output of the spectrograph, at the same time easing the spectral response requirements on the film, since the output phosphor emits only over a restricted wavelength range. Of course, a calibration spectrum from a suitable comparison source must also be recorded. Thus, in an échelle spectrograph, the cross-disperser must provide sufficient order separation to record a suitably widened spectrum plus adjacent comparison spectra (on both sides of the order) of sufficient width for precision wavelength determinations.

Elements of an Échelle Spectrograph

An entrance slit of width w and height h is placed at the common focus of the telescope and the collimator, of focal length f_1 and diameter d_1'. Parallel light from the collimator is dispersed by the échelle grating, whose grooves are parallel to the entrance slit, and in the perpendicular direction by the cross-disperser. The dispersed beams are collected by a camera of focal length

f_2, and sufficient aperture to avoid vignetting (the beams for different diffraction angles being physically separated), to form an image of the spectrum, each line of which is an image of the slit, of width w' and height h'. The projected slit width w' and height h' will vary with wavelength according to the diffraction angles.

If the telescope has focal length F and aperture D and hence focal ratio

$$f = F/D \qquad 3.1$$

then, by similar triangles, the collimator must have the same focal ratio, so that the diameter of the collimated beam for light from each point along the slit is

$$d_1 = f_1/f \quad . \qquad 3.2$$

since h is nonzero, the required collimator diameter d_1' for no vignetting will be slightly larger than d_1 as we will see later. Since $w < h$, it will have no effect in this regard.

Projected Slit Width and Resolution

As we expect, the resolution of the spectrograph seldom achieves, in practice, the theoretical limit given by equation 2.34, but is instead limited by the finite width of the entrance slit, or more precisely, that of its image, which is called the projected slit width.

Since the slit is of nonzero width w, the angle of incidence α on the échelle grating varies for light from

different parts of the slit, through an angle

$$\delta\alpha = w/f_1 \quad . \qquad 3.3$$

Differentiating the grating equation 2.2 with respect to α, we find, for fixed m, λ, γ:

$$\frac{d\beta}{d\alpha} = - \frac{\cos \alpha}{\cos \beta} \quad . \qquad 3.4$$

Hence the image of the slit subtends the angle

$$\delta\beta = \frac{\cos \alpha}{\cos \beta} \frac{w}{f_1} \qquad 3.5$$

which therefore represents the effective angular resolution of the spectrograph, by the Rayleigh criterion, mentioned earlier in connection with equation 2.31. Hence the angle $\delta\beta$ subtends a distance w' in the focal plane of the camera given by

$$w' = f_2 \delta\beta = w \frac{\cos \alpha}{\cos \beta} \frac{f_2}{f_1} \qquad 3.6$$

which, by definition, is the projected slit width. Thus w' represents the linear resolution of the spectrograph, and should therefore be chosen to match the resolving characteristics of the plate and/or image-tube to be used with the spectrograph.

If we insert the angle $\delta\beta$ given by equation 3.5 above into the dispersion equation 2.32, we find that the effective spectrograph resolution is

$$R = \frac{\lambda}{\delta\lambda} = \lambda \frac{\delta\beta}{\delta\lambda} \frac{\cos \beta}{\cos \alpha} \frac{f_1}{w} = \left(\frac{\sin \alpha + \sin \beta}{\cos \alpha}\right) \frac{f_1}{w} \quad . \qquad 3.7$$

Since $W \cos \alpha = d_1 = f_1/f$, we have, from equation 2.34, that the ratio of effective to theoretical resolution is

$$\frac{R}{R_o} = \frac{f}{\cos \gamma} \frac{\lambda}{w} \qquad 3.8$$

which is typically on the order of 10^{-1}, as we will see in the next chapter. Also, we remark that R given above is often called the spectral purity or chromatic resolution, in contradistinction to the (theoretical) resolution R_o.

Throughput

The spectrograph throughput is defined as the output flux relative to the source luminance (photometric brightness). Following Jacquinot (1954) and Schroeder (1970), if $R/R_o \leq \frac{1}{3}$, then diffraction effects can be ignored and the throughput L is the product of the normal area of the collimated beam, the solid angle subtended by the slit at the collimator, and the overall spectrograph transmittance τ_o. Hence,

$$L = \tau_o \left(\frac{\pi d_1^2}{4 f_1^2}\right) wh = \tau_o \left(\frac{\pi}{4 f^2}\right) wh = \tau_o \left(\frac{\pi D^2}{4}\right) \Psi' \Psi \qquad 3.9$$

where $\Psi' = w/F$, $\Psi = h/F$ are the angular dimensions of the slit in the focal plane of the telescope. From equation 3.6, and a similar one for h', we see, on consideration of Figure 2.1, that the throughput is also the product of the normal area of the diffracted beam (at the camera), the solid angle subtended by the image of the slit at the camera, and the overall transmittance τ_o.

Combining equations 3.7 and 3.9, we see that the product LR is

$$LR = \tau_o \frac{\cos \beta}{\cos \alpha} \left(\frac{\pi D \Psi}{4}\right) d_1 \lambda \frac{d\beta}{d\lambda} \quad . \qquad 3.10$$

Since the factor τ_o contains the échelle efficiency (2.94), which varies as $\cos \alpha / \cos \beta_B$, we see that if Ψ is taken as the angular diameter of the stellar seeing disk, then, for a given telescope, the product LR is jointly proportional to the collimator size and angular dispersion. Thus, for a given collimator size, an échelle spectrograph enjoys a considerable advantage in resolution and/or throughput over a conventional grating instrument, as stated in chapter one.

Plate Factor

Clearly, the linear distance dx in the focal plane of the camera, corresponding to the angle $d\beta$, is

$$dx = f_2 \, d\beta \quad . \qquad 3.11$$

Hence the linear dispersion can be written

$$\frac{dx}{d\lambda} = \frac{d\alpha}{d\beta} \frac{d\beta}{d\lambda} = f_2 \frac{d\beta}{d\lambda} \qquad 3.12$$

and from the dispersion equation 2.32 we therefore have that the reciprocal linear dispersion, or plate factor, is

$$P = \left(f_2 \frac{d\beta}{d\lambda}\right)^{-1} = \left(\frac{\cos \beta}{\sin \alpha + \sin \beta}\right) \frac{\lambda}{f_2} \qquad 3.13$$

which is usually expressed in Å/mm. Therefore, an échelle

spectrograph can obtain the same plate factor (a few Å/mm) as a conventional coudé spectrograph, but with a much shorter camera focal length. If the linear resolutions are also comparable, then from equation 3.6 we see that the collimator focal length f_1 will also be shorter in roughly the same proportion, and hence the échelle instrument will be much more compact, as stated in chapter one.

Spectral Line Tilt

We now investigate the effect of the parameter γ on the spectrograph output. Since $d\beta/d\gamma$ is the tangent of the angle between the focused image of the slit (spectral line) and the direction parallel to the échelle grooves, the spectral lines will be perpendicular to the direction of the échelle dispersion when $d\beta/d\gamma = 0$, and otherwise 'tilted' by an angle whose tangent is $d\beta/d\gamma$.

Differentiating the grating equation 2.2 with respect to γ, and using the dispersion equation 2.32, we find that, for constant m, λ, α:

$$\frac{d\beta}{d\gamma} = \tan\gamma\left(\frac{\sin\alpha + \sin\beta}{\cos\beta}\right) = \tan\gamma\left(\lambda\frac{d\beta}{d\lambda}\right) \quad . \qquad 3.14$$

Since the quantity in parentheses is not constant with wavelength, we see that unless $\gamma \equiv 0$, the orientation of the spectral lines will depend on their location on the focal surface. Thus, if the échelle grating is not mounted square with the collimator, or is preceded by a cross-dispersing element in the spectrograph, then the spectrum

will suffer from variable line tilt, typically over a range of several degrees.

Since variable line tilt enormously complicates the analysis of the spectrum, we will avoid it, by setting $\gamma = 0$ and placing the cross-disperser in the diffracted beam from the échelle. Under these conditions, $d\beta/d\gamma$ vanishes identically, and all spectral lines will therefore be perpendicular to the direction of the principal dispersion.

Order Separation

Due to considerations in the last chapter and others in the next, we will choose our cross-disperser to be a plane grating working in first order. The cross-dispersion grating has parameters $\alpha' = \phi' << 1$, β', γ', d' and $\lambda_B' = 2d'\sin\phi'$. Note that $\gamma' \neq 0$ will have no effect on the spectral lines, although it will influence the effective blazed wavelength $\lambda_{B'} = \cos\gamma\,\lambda_B'$.

Here we desire only a rough estimate of the échelle order separation in order to select a suitable cross-disperser from a list of standard gratings. Now, from the free spectral range equation 2.39 and the dispersion equation 2.32 we have that the angular separation of échelle orders m and $m \pm 1$ is approximately

$$\Delta\beta' = \Delta\lambda \frac{d\beta'}{d\lambda} \simeq \frac{\lambda}{m}\left(\frac{1}{d'\cos\gamma'\cos\beta'}\right) \simeq \frac{N'\lambda}{m} \quad . \qquad 3.15$$

If the grating constant N' is in grooves/mm and λ is in Å,

then

$$\Delta\beta' \simeq \frac{N'\lambda}{10^7 m} \quad . \qquad 3.16$$

Thus, to ensure adequate order separation, we must choose N' and the camera focal length f_2 such that the linear separation of the highest two orders of interest is

$$f_2\Delta\beta' \simeq 1 \text{ mm} \qquad (m = m_{max}\,,\ \lambda = \lambda_{min}) \quad . \qquad 3.17$$

This allows for widening the spectrum to about $\frac{1}{2}$ mm, leaving room for about $\frac{1}{4}$ mm of comparison spectra to be exposed on either side of each order. If λ_B' is then chosen so that the spectral region of interest lies between $\frac{1}{2}\lambda_B'$ and $\frac{3}{2}\lambda_B'$, then the blaze efficiency $B_o'(\beta')$ of the cross-disperser, as given by equation 2.14, will generally exceed 70%.

Exit Pupil Considerations

If a Cassegrain telescope has a (concave) primary mirror of (positive) focal length F_1 and a (convex) secondary mirror of (negative) focal length F_2, separated by a distance D_1, then the effective focal length of the telescope is

$$F = \frac{F_1F_2}{F_1 + F_2 - D_1} \qquad 3.18$$

and the focal plane is a distance D_2 from the secondary, where

$$D_2 = F\left(\frac{F_1 - D_1}{F_1}\right) \qquad 3.19$$

as stated by Gascoigne (1968). Also, the exit pupil of the telescope, defined as the (virtual) image of the primary in the secondary, is a distance G from the focal plane of the telescope, where

$$G = F\left(\frac{F_2}{F_2 - D_1}\right) \qquad 3.20$$

from the results of Harmer (1974), which we use in the remainder of this section. The exit pupil of the spectrograph, defined as the image of the telescope exit pupil in the collimator, is a distance g from the collimator, where

$$g = f_1(1 + f_1/G) \qquad 3.21$$

and has diameter d_1, as defined earlier in equation 3.2. Hence, if a slit of height h and width w is introduced into the common focal plane of the telescope and collimator, the collimated beam has height and width, respectively, of

$$h_1 = d_1 + \ell h/f_1 \qquad 3.22$$

$$w_1 = d_1 + \ell w/f_1 \qquad 3.23$$

at a distance ℓ from the collimator exit pupil. Similarly, if the Cassegrainian secondary diameter is qD, where q is the obstruction ratio of the telescope, then the completely silhouetted portion of the collimated beam has height and width, respectively, of

$$h_2 = qd_1 - \ell h/f_1 \qquad 3.24$$

$$w_2 = qd_1 - \ell w/f_1 \quad . \qquad 3.25$$

Generally, the terms in w are negligible, so that for all practical purposes we may set $w_1 = d_1$, $w_2 = qd_1$. Since $h > w$ in any case, the diameter of the collimator necessary to avoid vignetting is, from 3.21 and 3.22,

$$d_1' = d_1 + h(1 + f_1/G) \qquad 3.26$$

which will exceed d_1 by typically 1-2 mm (cf. equation 3.17) for échelle spectrographs.

These and some other relationships are illustrated in Figure 3.1, which also shows the specifications of the University of Alberta 20-inch telescope, in the f/8 classical Cassegrain configuration to be used with the spectrograph.

We now have all the formulae necessary to execute the design for our spectrograph, which we do in the next chapter.

Figure 3.1: Gaussian (first order) layout of Cassegrain telescope plus collimator. The collimator is shown as a lens for simplicity. Figures in parentheses are the design values for the University of Alberta 0.5 m telescope in the f/8 classical Cassegrain configuration. Figures in square brackets are the design values which will be set in chapter four. Note that d_1' exceeds the base of the constructed cone, of dimension d_1, by a small amount (see text). The vertical scale is twice the horizontal scale.

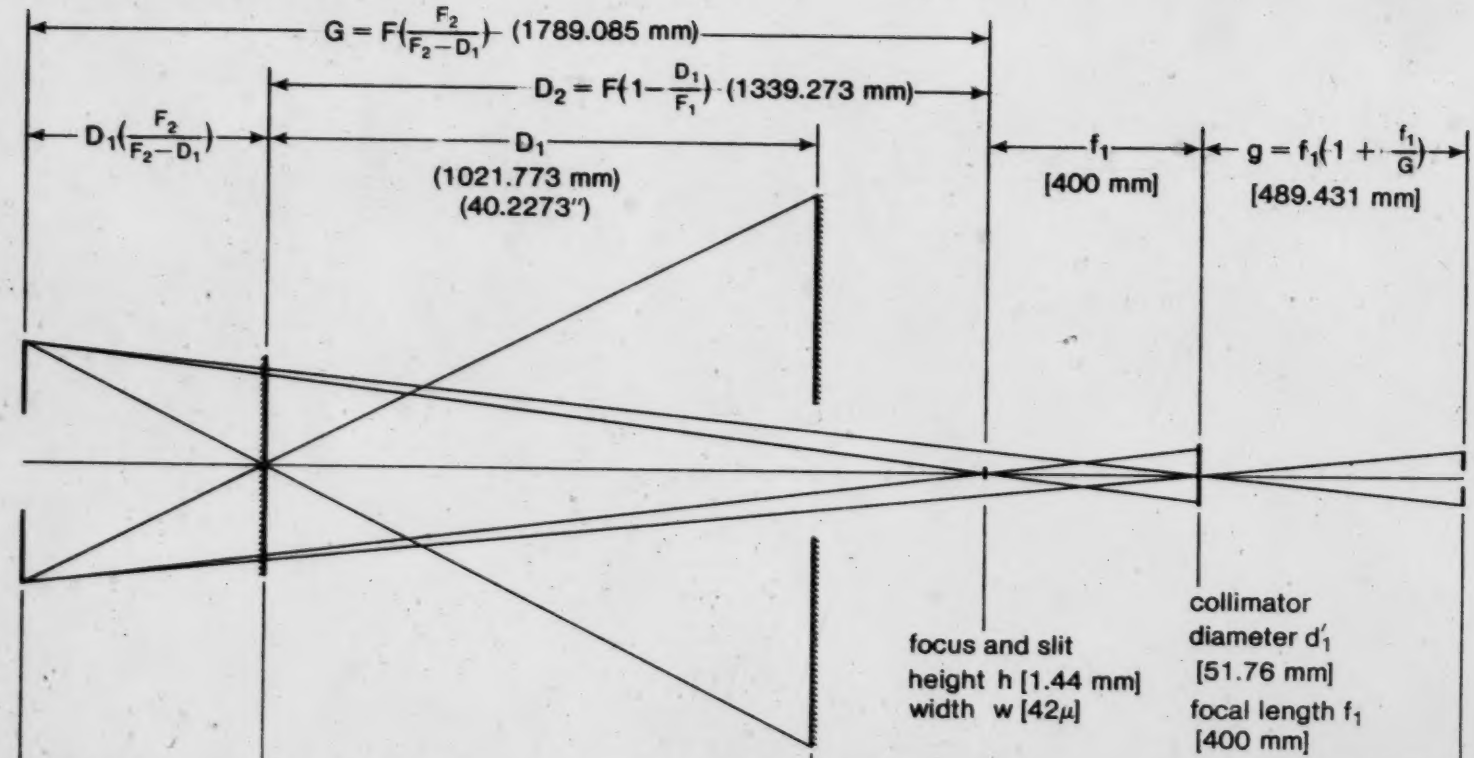
$G = F\left(\frac{F_2}{F_2 - D_1}\right)$ (1789.085 mm)
$D_2 = F\left(1 - \frac{D_1}{F_1}\right)$ (1339.273 mm)
$D_1\left(\frac{F_2}{F_2 - D_1}\right)$
D_1
(1021.773 mm)
(40.2273″)
f_1
[400 mm]
$g = f_1\left(1 + \frac{f_1}{G}\right)$
[489.431 mm]
focus and slit
height h [1.44 mm]
width w [42μ]
collimator
diameter d_1'
[51.76 mm]
focal length f_1
[400 mm]
(telescope)
exit pupil
outer diameter
$D\left(\frac{F_2}{F_2 - D_1}\right)$
inner diameter
$qD\left(\frac{F_2}{F_2 - D_1}\right)$
secondary mirror
diameter qD (203.2 mm) (8″)
focal length F_2(−803.564 mm)
(−31.6364″)
primary mirror
diameter D (508mm)(20″)
focal length F_1 (1524 mm) (60″)
(collimator)
exit pupil
outer diameter
$d_1 = f_1\left(\frac{D}{F}\right)$
[50 mm]
inner diameter
qd_1 [20 mm]
(telescope) effective focal length $F = \frac{F_1 F_2}{F_1 + F_2 - D_1}$ (4064 mm) (160″)

CHAPTER 4

SPECTROGRAPH DESIGN

In choosing our spectrograph design, the prime consideration is to have instrument performance limited by the astronomical seeing or detector resolution, and not by the geometrical aberrations of the spectrograph elements. Therefore, a reasonable spectrograph design for an f/8 telescope must be based on a choice of a collimator and camera which are both essentially abberation free, at least over their respective field diameters.

We will defer selection of the camera design to the next chapter, since our choice will be largely dictated by its required aperture, focal length and field coverage. Since we have already selected an échelle grating as our principal dispersive element, it remains to choose a suitable collimator and cross-disperser, before we proceed to detailed calculations.

Choice of Collimator

Since the dimensions of the slit limit the field coverage of the collimator to about 1 mm diameter (see the discussion following equation 3.17), and the collimator works at an effective focal ratio of f/8 (from Figure 3.1 and equation 3.2), a simple paraboloidal mirror can be used to collimate the light from the telescopic stellar

image with negligible aberrations.

The choice therefore rests between an off-axis paraboloid and one used on-axis with a folding flat, in a Newtonian arrangement. We note that, because of the secondary obstruction of the telescope ($q = 0.4$ from Figure 3.1), this diagonal mirror will not vignette the collimator beam whatsoever.

For our purposes, the on-axis paraboloid is to be preferred, since it allows the long dimension of the spectrograph to be placed parallel to the telescope tube (see Introduction), and, for a given field diameter, it has smaller aberrations (Schroeder (1970)). Of course, a plane mirror can introduce no aberrations to an optical system, so the only disadvantage offered by our choice is a slight loss of light due to the extra reflection at the diagonal.

Choice of Cross-Disperser

Since the minimum order separation is about 1 mm (see the discussion following equation 3.17), the 40 mm diameter of a standard image-tube photocathode will only accept about 2000-3000 Å of spectrum. Thus, the spectrograph output must be divided into two wavelength ranges, requiring different amounts of cross-dispersion to optimize the output format.

The short wavelength limit should be chosen to lie between atmospheric cutoff, near 3100 Å, and the Balmer

limit, at about 3600 Å. The long wavelength limit should correspond to that of the spectral response of the image-tube photocathode. For an S-20 (or equivalent) photocathode, this is ~8500 Å, while for an S-25 (extended red) or GaAs photocathode, the limit is ~8900 Å.

If the spectrograph is to be used without an image-tube, the long-wavelength limit will be determined by the limit of the spectral response of the emulsion. For Kodak I-N spectroscopic plates (see chapter six), this limit is also about 8900 Å. In this case, to capture the entire spectrum in a single exposure would require tripling the field coverage of the camera. Since IIa-D is superior to I-N for $\lambda \lesssim 6400$ Å in any case, it is a good idea to divide the output into two wavelength regions here, as well.

In order to avoid variable spectral line tilt (see the discussion accompanying equation 3.14), we require all cross-dispersion to be done on the diffracted beam from the échelle. Since, in general, prisms have inadequate dispersive power and holographic gratings are too inefficient, our cross-disperser must be a standard plane transmission or reflection grating. Since the blaze direction of a transmission grating is that at which a prism of apex angle ϕ' would disperse the light, the entire camera would have to be rotated, through an axis on the grating face, to different positions for each wavelength range. For reasons of rigidity and permanence of alignment, it is much better to mount the camera in a fixed position. Therefore,

since transmission gratings offer no compensating advantages in return for abandoning the use of a fixed camera, our cross-disperser for each range will be a plane reflection grating.

Although it would be more economical to use a single grating, in first and second orders, for the two wavelength ranges, we will employ two different gratings, both used in first order, as the cross-dispersers, for the following reasons: First, as described earlier, there are practical difficulties in filtering out unwanted light of longer wavelengths when using a grating in second order. Second, the optimum choice of blaze wavelengths λ_B' for each wavelength range will not be in the ratio 2:1, but about 1.6:1. Third, as can be seen from Figure 2.2, the width of the blaze peak in second order is much less than that in first order. Fourth, using two separate gratings allows them to be set into interchangeable mounts, each permanently aligned, and avoid the necessity of rotating a single grating to two different positions.

Orientation of Échelle

It is convenient to mention here the reasons for using the échelle in the $\alpha > \beta$ orientation, rather than the reverse. First, from equations 3.2 and 3.7, we can write the resolution as

$$R = \frac{\lambda}{\delta\lambda} = \left(\frac{\sin\alpha + \sin\beta}{\cos\alpha}\right) \frac{fd_1}{W} \quad . \qquad 4.1$$

Hence, for a fixed collimator size d_1 and slit width w, higher resolution is obtained for $\alpha > \beta$. Second, since the diffracted beam diameter is, from Figure 2.1, $d_2 = d_1(\frac{\cos\beta}{\cos\alpha})$, we can rewrite equation 3.13 for the plate factor (reciprocal linear dispersion) as

$$P = (f_2 \frac{d\beta}{d\lambda})^{-1} = (\frac{\cos\alpha}{\sin\alpha + \sin\beta}) \frac{\lambda}{f' d_1} \qquad 4.2$$

where $f' = f_2/d_2$ is the effective focal ratio of the camera. Hence, for fixed d_1 and f'; a lower plate factor (higher linear dispersion) is obtained for $\alpha > \beta$. [We remark that since equation 3.6 for the projected slit width w' can be rewritten as

$$\frac{w'}{w} = \frac{f'}{f} \qquad 4.3$$

we have that for fixed w' (chosen to match the resolution characteristics of the detector), and fixed w (chosen to match the diameter of the seeing disc), f' is also fixed.] Third, as mentioned earlier, having $\alpha > \beta$ avoids shadowing of the grooves, and the consequent loss of échelle efficiency.

Selection of Échelle Groove Spacing and Blaze Angle

For economical reasons, our échelle grating will be a replica of a currently available master. In order to obtain the best available quality, we will select our échelle from the list of rulings offered by Bausch & Lomb,

shown in Table 4.1. Although only those gratings marked standard (std) are available in large sizes, all those listed are available in the smaller sizes suitable for a Cassegrain spectrograph such as the one we are designing here.

Catalogue Number	N	ϕ (blaze)	
35-13-*-411	31.6	63°26' (R-2)	(std)
35-13-*-415	52.67	63°26' (R-2)	
35-13-*-401	79	63°26' (R-2)	(std)
35-13-*-402	79	75°58' (R-4)	
35-13-*-403	98.76	63°26' (R-2)	
35-13-*-451	316	63°26' (R-2)	(std)

Table 4.1: Bausch & Lomb échelles. N is listed in grooves/mm, and the blaze designations correspond to tan ϕ (e.g. R-2 means tan $\phi = 2$). The asterisk is replaced by the desired size code when ordering. Standard (std) gratings are available in large sizes.

Now since the spectral region to be covered is divided into two wavelength ranges, each with a grating cross-disperser providing ~1 mm minimum order separation, and all the orders of each range must be contained within the 40 mm field diameter covered by a standard image-tube, we have that the maximum and minimum order numbers must differ by

$$m_{max} - m_{min} \simeq 40 \quad . \qquad 4.4$$

Of course, for other spectrograph designs, this number will be proportional to field diameter and the number of wavelength ranges, and vary inversely with the minimum order separation. Neglecting the factor cos θ in equation 2.27 (cos γ = 1 since we have chosen γ = 0 to avoid spectral line tilt), we can write

$$m_{max} \approx \frac{2d \sin \phi}{\lambda_{min}} = \frac{2 \cdot 10^7 \sin \phi}{N \lambda_{min}} \qquad 4.5$$

$$m_{min} \approx \frac{2d \sin \phi}{\lambda_{max}} = \frac{2 \cdot 10^7 \sin \phi}{N \lambda_{max}} \qquad 4.6$$

where the latter equalities are for N in grooves/mm and λ in Å. Due to the angular size $2\Delta\beta_E$ of the échelle orders, it will turn out that our camera will need to employ a full-aperture correcting plate of the Schmidt type. In order to reach atmospheric cutoff at about 3100 Å, such a corrector would need to be made of quartz (fused silica) and hence be very expensive. However, by using instead a low dispersion crown glass of enhanced ultraviolet transmittance, UBK-7, we can make a substantial savings without losing too much spectral coverage. Since the transmittance of UBK-7 begins to fall off fairly quickly shortward of 3400 Å, we will use this as λ_{min}. Also, since the spectral response of the image-tube (or I-N plate) begins to fall off rapidly longward of 8800 Å, we will use this figure as λ_{max}. Performing the necessary calculations, we find the results in Table 4.2 below:

N (blaze)	m_{max}	m_{min}	$m_{max}-m_{min}$	
31.6 (R-2)	166.5→166	64.3→65	101	
52.67 (R-2)	99.9→100	38.6→39	61	
79 (R-2)	66.6→ 66	25.7→26	40	(*)
79 (R-4)	72.2→ 72	27.9→28	44	(*)
98.76 (R-2)	53.3→ 53	20.6→21	32	(*)
316 (R-2)	16.6→ 16	6.4→ 7	9	

Table 4.2: $m_{max}-m_{min}$ for the échelles shown in Table 4.1, corresponding to $\lambda_{min} = 3400$ Å, $\lambda_{max} = 8800$ Å.

Thus, we must choose our échelle from among the starred (*) gratings.

Before we proceed further, we need a method of estimating θ. For maximum compactness, we will place the échelle a short distance $\ell' \simeq \frac{1}{2}d_1$ inside the focus of the collimator. From equation 3.21 and Figure 3.1, it will then also be not too far from the collimator exit pupil, as recommended by Harmer (1974). The final arrangement of the optical components is shown in Figure 4.3. Referring to this figure, we see that the angle ξ subtended by the collimator at the nearer edge of the échelle is approximately

$$\xi \simeq \tan\xi = \frac{d_1'}{f_1 - \ell' - \frac{1}{2}d_1 \tan\alpha} \gtrsim \frac{2}{2f - 1 - \tan\phi} \qquad 4.7$$

where f is the common effective focal ratio of the collimator and telescope. For no vignetting, we must have $2\theta > \xi + (\Delta\beta_E)_{max}$. At the same time, θ must be kept small to maximize the efficiency (2.94) of the échelle. But, from equation 2.64, we have

$$(\Delta\beta_E)_{max} = \frac{\tan\phi}{m_{min}(1 + \tan\theta\tan\phi)} \lesssim \frac{\tan\phi}{m_{min}} \quad . \qquad 4.8$$

Therefore, we can estimate θ as

$$\theta \simeq \frac{\tan\phi}{2m_{min}} + \frac{1}{2f - 1 - \tan\phi} \quad . \qquad 4.9$$

This result is used with equation 4.7 to determine the camera focal length f_2 that gives a maximum échelle order length of ~90% of the full field diameter, i.e., in our case:

$$f_2(\Delta\beta_E)_{max} \simeq 18 \text{ mm} \quad . \qquad 4.10$$

Finally, we set $w = 40\ \mu$, or 2" arc in the focal plane of the telescope, and (since the approximately 12-15 μ resolution of IIa-D (and I-N) depends on development) we set $w' \simeq 18\ \mu$, to avoid emulsion-limited resolution. These choices then fix all the other spectrograph parameters. Using equation 4.3, we find

$$f_1 = f_2 \frac{w}{w'} \left(\frac{\cos\alpha}{\cos\beta_B}\right) = 2.22\, f_2 \left(\frac{\cos\alpha}{\cos\beta_B}\right) \quad . \qquad 4.11$$

Since $d_1 = f_1/f = f_1/8$, we have that the required width of the échelle is

$$W = d_1/\cos\alpha = f_1/8\cos\alpha \qquad 4.12$$

Also, since $d_2 = W\cos\beta_B = f_2/f' \simeq f_2/3.6$, we have that the required length of the cross-dispersion grating is approximately

$$W' = f_2/3.6 + 2f_1(\Delta\beta_E)_{max} \ . \qquad 4.13$$

Finally, since the other factors in the throughput (3.9) are fixed, the intensity of the spectrograph output will vary as the échelle efficiency (2.94). On the blaze, this is given by equation 2.93, while at the end of the échelle orders, we have, using equation 2.61, that the échelle efficiency is

$$E(\beta^*) = \left(\frac{\cos\alpha}{\cos\beta_B}\right)\,\mathrm{sinc}^2\left[\frac{\pi}{2}\left(\frac{\cos\alpha}{\cos\beta_B}\right)\right] \ . \qquad 4.14$$

These calculations are carried out for the échelles selected from Table 4.2 and the results are presented in Table 4.3(a), below:

equation: (4.9) (4.8) (4.10) (4.11) (4.12) (4.13) (4.1) (4.2) (2.93) (4.14)

N (blaze)	θ	$(\Delta\beta_E)_{max}$	f_2	f_1	W	W'	R ($\cdot 10^3$)	P (Å/mm)	$E(\beta_B)$	$E(\beta^*)$	
79 (R-2)	6.6°	3.6°	288	400	145	130	52	5.34	62%	45%	(1a)
79 (R-4)	9.3°	5.0°	208	97	145	75	56	4.94	21%	20%	(2a)
98.76 (R-2)	7.1°	4.4°	236	315	118	114	42	6.62	60%	44%	(3a)

Table 4.3(a): Approximate spectrograph parameters for an échelle-collimator separation of $(f_1 - \ell')$. All linear dimensions are in mm. R and P are for $\beta = \beta_B$, and P is at $\lambda = 5000$ Å.

If we decrease the value of θ (to improve the efficiencies $E(\beta_B)$ and $E(\beta^*)$) by increasing the échelle-collimator separation to $2f_1$ (i.e. by placing the échelle at the center of curvature of the collimator), and make the appropriate changes to equations 4.9 and 4.13, we obtain the results of Table 4.3(b), below:

N (blaze)	θ	$(\Delta\beta_E)_{max}$	f_2	f_1	W	W'	R ($\cdot 10^3$)	P (Å/mm)	$E(\beta_B)$	$E(\beta^*)$	
79 (R-2)	4.1°	3.9°	266	443	145	134	52	5.34	75%	46%	(1b)
79 (R-4)	6.1°	5.7°	180	160	145	82	56	4.94	40%	35%	(2b)
98.76 (R-2)	4.6°	4.7°	220	353	118	118	42	6.62	72%	46%	(3b)

Table 4.3(b): Approximate spectrograph parameters for an echellé-collimator separation of $(2f_1)$. All linear dimensions are in mm. R and P are for $\beta = \beta_B$, and P is at $\lambda = 5000$ Å.

Clearly, of the three designs in Table 4.3(a), design (1a) is the best. Although design (2a) offers about 8% higher resolution and dispersion, it is only about 40% as efficient. Also, although design (1a) is the least compact, its total internal length, $\sim(f_1 + f_2) \approx 0.69$ m, easily meets our requirements, and any further reduction in size, at the expense of performance, would be foolish.

We now compare each of the designs in Table 4.3(b) to design (1a). We note that the increased efficiency $E(\beta_B)$ in design (1b) only serves to make the blaze

distribution more non-uniform, and it is not worth the 67% increase in total internal length, which is now $\sim(2f_1 + f_2) \simeq 1.15$ m, and over the size limit mentioned in the Introduction. The échelle efficiency of design (2b), though almost twice that of (1b), is still low, while the increased field coverage required of the camera, about 12.5° ($2.2(\Delta\beta_E)_{max}$) is about 60% larger than the 7.9° field coverage required of the camera in design (1a), implying greater difficulties in controlling the camera aberrations, in the former case. Design (3b) essentially combines the faults of designs (1b) and (2b), only to a lesser degree, and also performs with about 20% less resolution and dispersion than design (1a).

Thus, the best spectrograph design is obtained by selecting the 79 gr/mm R-2 grating as the échelle, and using the compact configuration, with the échelle just inside the collimator focus.

Selection of Cross-Disperser Groove Spacing and Blaze Wavelength

Again here, our cross-dispersers will be replica gratings chosen from the list of rulings available from Bausch & Lomb.

For the short wavelength range, we have from equations 3.16 and 3.17 the condition that N', in grooves/mm, is roughly

$$N' \simeq \frac{10^7 m_{max}}{f_2 \lambda_{min}} \qquad 4.15$$

where f_2 is in mm and λ_{min} is in Å. Using the data for design (1a) from the previous section (i.e. $m_{max} = 66$, $\lambda_{min} = 3400$ Å, $f_2 = 288$ mm), we find

$$N' \simeq 674 \text{ gr/mm} . \qquad 4.16$$

Thus, we will use a 600 gr/mm grating, blazed at 4000 Å, for our cross-disperser for the short wavelength range. This grating allows us to fit orders 66-42, and part of 41, within a 40 mm diameter field. Hence the short wavelength range is about 3400-5500 Å. These limits correspond to cross-disperser blaze efficiencies of about 90% and 77%, respectively.

The long wavelength range is therefore from orders 41 to 26, corresponding to about 5400-8800 Å. Setting $m_{max} = 41$ and $\lambda_{min} = 5400$ Å in formula 4.15 (and keeping f_2 the same), we find

$$N' \simeq 264 \text{ gr/mm} . \qquad 4.17$$

Thus, we will use a 300 gr/mm grating, blazed at 6400 Å, for our cross-disperser for the long wavelength range. The wavelength limits given above then again correspond to cross-disperser blaze efficiencies of about 90% and 77%, respectively.

We note that since the standard gratings do not have the grating constants N' required by formula 4.15,

the minimum order separations will vary from 1 mm. In the short wavelength range case, it will be about 600/674 mm or 0.9 mm. Hence, if h' is set equal to 1 mm, adjacent comparison spectra for about the highest four orders will overlap slightly ($\lesssim 0.1$ mm). However, this small overlap is unlikely to cause any confusion in interpreting the spectra.

Optimizing the Blaze of Hα, Hβ, Hγ, Hδ and K lines

The hydrogen lines Hα, Hβ, Hγ and Hδ and the calcium K line are very important in stellar spectroscopy, and are often extensively broadened. For these reasons we would like to have them located near the central blaze of their respective échelle orders, and not near the 'ends'. In order to thus optimize the blaze for each of these wavelengths λ, we select the (smallest) value of θ which renders the effective order numbers

$$m_{eff} \equiv \frac{d \cos\gamma (\sin\alpha + \sin\beta_B)}{\lambda} = \frac{2d \cos\gamma \sin\phi \cos\theta}{\lambda} \qquad 4.18$$

as close to integers as feasible. [From the grating equation 2.2, it is obvious that $m_{eff} = m$ for blazed wavelengths, while for 'end wavelength', λ^*,

$$\lambda^* \simeq \frac{d \cos\gamma (\sin\alpha + \sin(\beta_B \pm \Delta\beta))}{\bar{m} \pm \frac{1}{2}}$$

$$\simeq \frac{d \cos\gamma (\sin\alpha + \sin\beta_B)}{\bar{m}} \qquad 4.19$$

from equations 2.59 and 2.60, so that $m_{eff} \simeq \bar{m} = m \mp \frac{1}{2}$.] Since we have chosen $\gamma = 0$ to avoid spectral line tilt, $N = d^{-1} = 79$ grooves/mm, and $\phi = \arctan 2 = 63.435°$, the effective order numbers are

$$m_{eff} = \frac{226437.3 \text{ Å} \cdot \cos\theta}{\lambda} \qquad 4.20$$

Using the wavelengths published in the Handbook of Optics (1978), we compute m_{eff} for selected values of θ. The results are shown in Table 4.4 below:

line	λ(Å)	θ=6.6°	θ=6.7°	θ=6.8°	θ=6.9°	θ=7.0°	θ=7.1°	θ=7.2°
Hα	6562.808	34.274	34.267	34.260	34.253	34.246	34.239	34.231
Hβ	4861.342	46.270	46.261	46.252	46.242	46.232	46.222	46.212
Hγ	4340.475	51.823	51.813	51.802	51.791	51.780	51.769	51.757
Hδ	4101.748	54.839	54.828	54.817	54.805	54.794	54.782	54.770
K	3933.682	57.182	57.171	57.159	57.147	57.135	57.122	57.110
$\lvert m-m_{eff}\rvert$ rms :		0.2183	0.2160	0.2140	0.2126	0.2114	0.2108	0.2109
$E(\beta_B)$:		62.4%	62.0%	61.5%	61.0%	60.6%	60.1%	59.7%

Table 4.4: Effective order numbers, m_{eff}, for Hα, Hβ, Hγ, Hδ and K lines. The rms deviations from the (nearest) order numbers and the échelle efficiency $E(\beta_B)$ corresponding to each value of θ are also shown.

From the table, we can see that, taking the échelle efficiency into account, the spectral lines shown are optimally blazed at about $\theta = 7.0°$, which we therefore adopt as our value of θ.

Detailed Computation of the Final Design

Of the grating parameters, only the cross-disperser angles α' and γ' are undetermined. In order to maximize the cross-disperser grating efficiency, we choose

$$\alpha' = \beta'_B = \phi' = \arcsin(\lambda'_B/2d') \quad . \qquad 4.21$$

This angle is 6.892° for the 600 gr/mm, 4000 Å cross-disperser (short wavelength range), and 5.509° for the 300 gr/mm, 6400 Å cross-disperser (long wavelength range). Since the cross-disperser has its grooves perpendicular to those of the échelle, it is obvious that γ' varies according to

$$\gamma' = \text{constant} - \beta \quad . \qquad 4.22$$

Since we must have $\gamma' > \theta - \frac{1}{2}(\Delta\beta)_{max}$ when $\beta - \beta_B = (\Delta\beta)_{max}$ in order to avoid vignetting of the cross-dispersed beam by the échelle, and $\theta + \frac{1}{2}(\Delta\beta)_{max} \simeq 8.8°$, for the long wavelength range, in this case we set

$$\gamma' = 9° - (\beta - \beta_B) \quad . \qquad 4.23$$

(The extra angular margin is made to avoid vignetting by the unruled edge of the échelle blank.) Since the value of γ' has no influence on grating efficiency, provided it is not so large as to introduce polarization effects, we conveniently choose equation 4.23 to apply in the short wavelength range case, as well.

For each order, we first compute the angles β^* at the ends of the orders, from equations 2.59 and 2.78. We then use the grating equation 2.2 (or, equivalently, equation 2.66) to compute the corresponding wavelengths λ^*, which are shown, in the tables that follow, adjacent to the blazed wavelength (2.27) for that order. For each of these wavelengths, the grating equation for the appropriate cross-disperser is rearranged to give

$$\beta' = \arcsin\left(\frac{\lambda}{d' \cos \gamma'} - \sin \alpha'\right) . \qquad 4.24$$

The results for the short wavelength range are tabulated in Table 4.5, and the corresponding output format is shown in Figure 4.1. The results for the long wavelength range similarly appear in Table 4.6 and Figure 4.2. Note that since the dispersions of the échelle and cross-disperser are both proportional to $1/\lambda$, the ends of the échelle orders fall along straight lines in the spectrograph images, as shown in Figures 4.1 and 4.2. This fact greatly simplifies plotting. We have also included in Figures 4.1 and 4.2 the positions of the Hα, Hβ, Hγ, Hδ and K lines, as well as the Helium-Neon laser line at 6328 Å, which conveniently falls almost exactly at an end wavelength. Thus a small, inexpensive He-Ne laser will provide two equally bright spectral lines, which can be registered with marks on a reticle inserted in the camera focal plane, allowing the spectrograph to be thereby aligned and (coarsely) focused in a simple, effective manner. The

m	$\beta-\beta_B$	$\beta'-\beta_B'$	λ	m	$\beta-\beta_B$	$\beta'-\beta_B'$	λ
	-1.3854	-1.9510	3379.192		-1.5486	-0.5482	3776.605
66	0.0000	-1.9086	3405.296	59	0.0000	-0.4954	3809.314
	1.4023	-1.8624	3430.768		1.5698	-0.4371	3841.138
	-1.4065	-1.7692	3430.767		-1.5751	-0.3200	3841.138
65	0.0000	-1.7256	3457.685	58	0.0000	-0.2653	3874.992
	1.4240	-1.6778	3483.941		1.5970	-0.2049	3907.914
	-1.4284	-1.5817	3483.941		-1.6025	-0.0836	3907.914
64	0.0000	-1.5367	3511.712	57	0.0000	-0.0271	3942.974
	1.4464	-1.4874	3538.789		1.6252	0.0356	3977.053
	-1.4509	-1.3883	3538.789		-1.6309	0.1613	3977.053
63	0.0000	-1.3418	3567.453	56	0.0000	0.2198	4013.385
	1.4695	-1.2909	3595.391		1.6545	0.2849	4048.681
	-1.4741	-1.1885	3595.390		-1.6603	0.4152	4048.681
62	0.0000	-1.1406	3624.993	55	0.0000	0.4759	4086.355
	1.4934	-1.0879	3653.832		1.6848	0.5434	4122.937
	-1.4981	-0.9821	3653.832		-1.6909	0.6786	4122.937
61	0.0000	-0.9327	3684.419	54	0.0000	0.7415	4162.028
	1.5180	-0.8782	3714.205		1.7162	0.8117	4199.966
	-1.5229	-0.7688	3714.204		-1.7225	0.9521	4199.966
60	0.0000	-0.7177	3745.826	53	0.0000	1.0174	4240.557
	1.5435	-0.6614	3776.605		1.7488	1.0903	4279.928

Table 4.5: (Cont'd on page 64)

m	$\beta-\beta_B$	$\beta'-\beta_B'$	λ	m	$\beta-\beta_B$	$\beta'-\beta_B'$	λ
	-1.7554	1.2362	4279.928		-1.9823	3.2054	4831.861
52	0.0000	1.3040	4322.106	46	0.0000	3.2919	4885.860
	1.7827	1.3800	4362.993		2.0171	3.3901	4937.990
	-1.7895	1.5317	4362.992		-2.0259	3.5857	4937.990
51	0.0000	1.6022	4406.854	45	0.0000	3.6760	4994.434
	1.8179	1.6812	4449.345		2.0624	3.7790	5048.884
	-1.8250	1.8392	4449.344		-2.0715	3.9837	5048.883
50	0.0000	1.9125	4494.991	44	0.0000	4.0782	5107.944
	1.8545	1.9949	4539.183		2.1096	4.1862	5164.871
	-1.8619	2.1594	4539.183		-2.1192	4.4008	5164.870
49	0.0000	2.2357	4586.725	43	0.0000	4.4997	5226.733
	1.8927	2.3217	4632.723		2.1591	4.6131	5286.310
	-1.9004	2.4933	4632.723		-2.1692	4.8382	5286.310
48	0.0000	2.5727	4682.282	42	0.0000	4.9419	5351.179
	1.9324	2.6626	4730.198		2.2110	5.0611	5413.596
	-1.9405	2.8416	4730.198		-2.2215	5.2977	5413.595
47	0.0000	2.9245	4781.905	41	0.0000	5.4064	5481.696
	1.9739	3.0184	4831.862		2.2634	5.5320	5547.160

Table 4.5: Échelle order characteristics for short wavelength range. $N = 79$ grooves/mm, $\phi = 63.435°$, $\theta = 7°$, $\beta_B = 56.435°$, $\gamma = 0°$. $N' = 600$ grooves/mm, $\phi' = 6.892° = \beta_B'$, $\gamma' = 9° - (\beta-\beta_B)$. (All angles are shown in degrees and wavelengths are in Å).

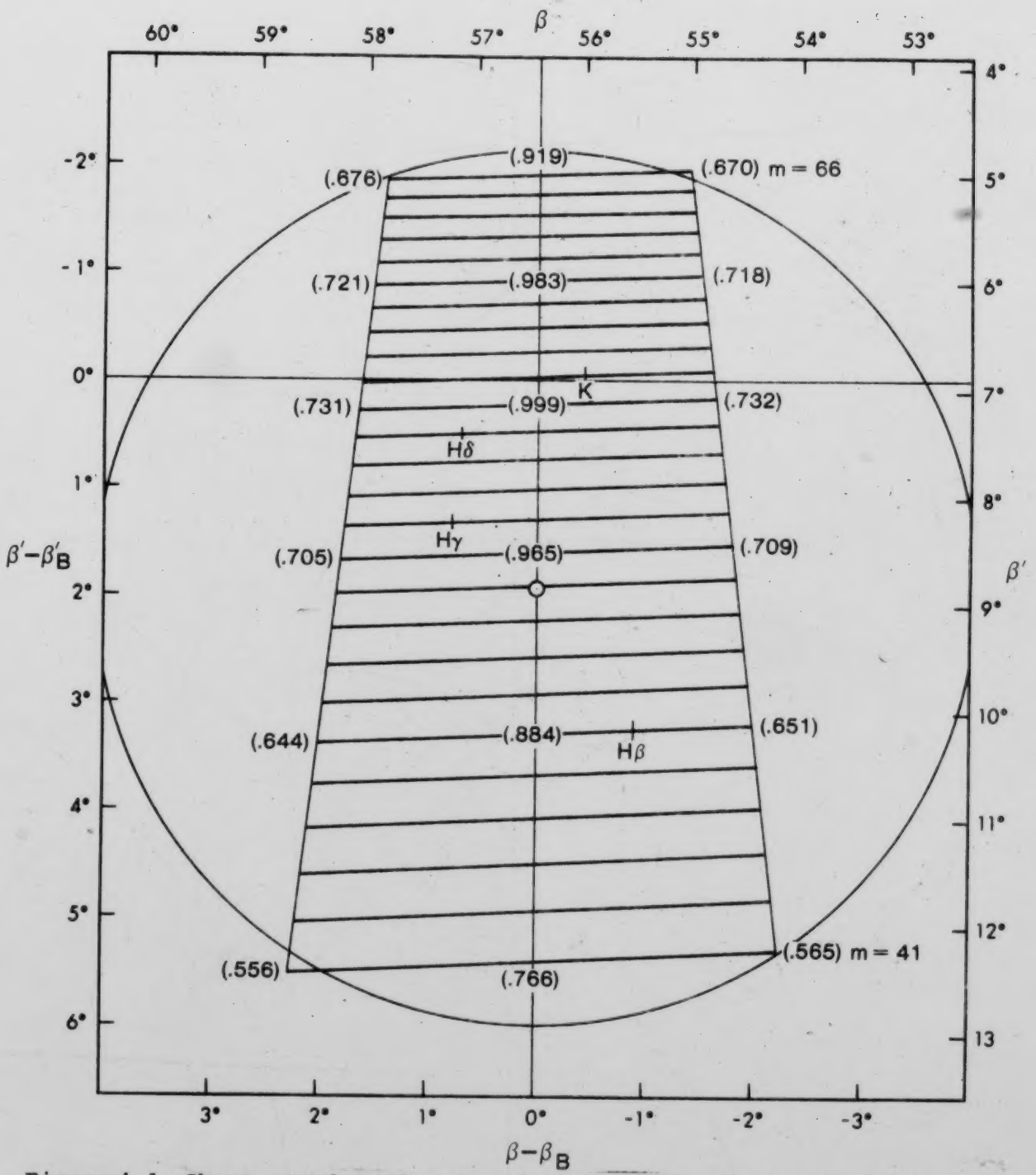

Figure 4.1: Short wavelength range image. Circle shows required field coverage of the image-tube, and center of circle indicates the direction of the camera's optical axis. Circle radius 4°04', center $\beta - \beta_B = 0°$, $\beta' - \beta'_B = 1°56'$. The combined blaze efficiency $B_1(\beta)B_o(\beta')$ is shown in parentheses for selected points.

m	$\beta-\beta_B$	$\beta'-\beta'_B$	λ	m	$\beta-\beta_B$	$\beta'-\beta'_B$	λ
	-2.1692	-1.7449	5286.310		-2.5265	-0.2054	6154.499
42	0.0000	-1.6940	5351.179	36	0.0000	-0.1369	6243.043
	2.2110	-1.6356	5413.596		2.5834	-0.0562	6327.690
	-2.2215	-1.5196	5413.595		-2.5978	0.1026	6327.688
41	0.0000	-1.4664	5481.696	35	0.0000	0.1750	6421.415
	2.2654	-1.4049	5547.160		2.6580	0.2606	6510.902
	-2.2765	-1.2831	5547.159		-2.6733	0.4289	6510.901
40	0.0000	-1.2272	5618.738	34	0.0000	0.5054	6610.280
	2.3226	-1.1625	5687.478		2.7371	0.5963	6705.035
	-2.3342	-1.0345	5687.477		-2.7532	0.7750	6705.033
39	0.0000	-0.9758	5762.809	33	0.0000	0.8560	6810.592
	2.3827	-0.9075	5835.076		2.8210	0.9529	6911.092
	-2.3950	-0.7727	5835.075		-2.8381	1.1429	6911.090
38	0.0000	-0.7110	5914.461	32	0.0000	1.2289	7023.423
	2.4461	-0.6389	5990.535		2.9101	1.3322	7130.208
	-2.4590	-0.4967	5990.534		-2.9284	1.5346	7130.205
37	0.0000	-0.4318	6074.312	31	0.0000	1.6261	7249.985
	2.5129	-0.3556	6154.501		3.0052	1.7366	7363.662

Table 4.6: (Cont'd on page 67)

m	$\beta-\beta_B$	$\beta'-\beta'_B$	λ
30	-3.0247	1.9527	7363.659
	0.0000	2.0501	7491.651
	3.1066	2.1686	7612.909
29	-3.1274	2.3999	7612.906
	0.0000	2.5039	7749.984
	3.2151	2.6312	7879.607
28	-3.2374	2.8794	7879.604
	0.0000	2.9906	8026.769
	3.3314	3.1279	8165.652
27	-3.3554	3.3948	8165.648
	0.0000	3.5141	8324.057
	3.4565	3.6624	8473.228
26	-3.4824	3.9504	8473.223
	0.0000	4.0787	8644.213
	3.5914	4.2396	8804.857

Table 4.6: Échelle order characteristics for long wavelength range. N = 79 grooves/mm, $\phi = 63.435°$, $\theta = 7°$, $\beta_B = 56.435°$, $\gamma = 0°$. N' = 300 grooves/mm, $\phi' = 5.509° = \beta'_B$, $\gamma' = 9° - (\beta - \beta_B)$. (All angles are in degrees and wavelengths are in Å).

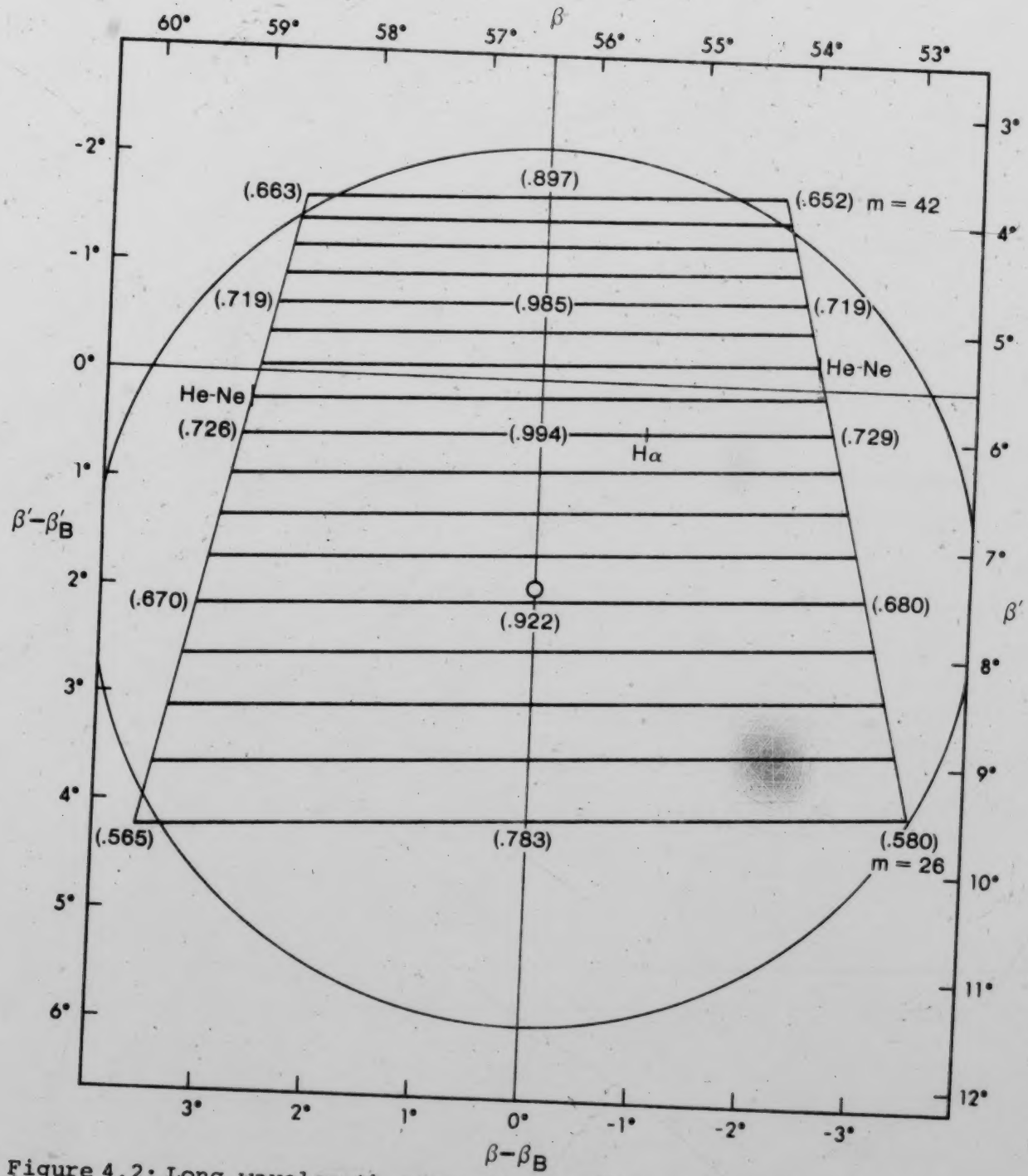

Figure 4.2: Long wavelength range image. Circle shows required field coverage of the image-tube, and center of circle indicates the direction of the camera's optical axis. Circle radius 4°04', center $\beta - \beta_B = 0°$, $\beta' - \beta_B' = 1°56'$. The combined blaze efficiency $B_1(\beta)B_o(\beta')$ is shown in parentheses for selected points.

combined blaze efficiency $B_1(\beta)B_o'(\beta')$ is shown at selected points in Figures 4.1 and 4.2, to give an indication of the intensity distribution over the images.

We now compute the remaining spectrograph parameters. From Figures 4.1 and 4.2, we see that the required field coverage is 8°08' (0.142 radian), which corresponds to a linear field diameter of 39 mm (allowing 1 mm for h') provided the camera focal length is

$$f_2 = 39 \text{ mm}/0.142 = 275 \text{ mm} \qquad 4.25$$

or 10.83 inches. From equations 4.11 and 4.12, this corresponds to an échelle width of about 138 mm. The closest (larger) standard size is 152 mm (6 inches) which gives

$$d_1 = W\cos\alpha = 152 \text{ mm } \cos(70.435°) = 50.9 \text{ mm}. \qquad 4.26$$

Since the échelle would need to be precisely centered as well as oriented to use this beam diameter, we will allow a small centering tolerance and set

$$d_1 = 50 \text{ mm} \qquad f_1 = fd_1 = 400 \text{ mm} \qquad 4.27$$

where the telescope/collimator focal ratio f = 8. From equation 3.6, we compute the projected slit width for w = 42 μ (2.1" arc in the telescope focal plane) as

$$w' = w\left(\frac{\cos\alpha}{\cos\beta_B}\right)\frac{f_2}{f_1}\cdot\left(\frac{\cos\beta_B}{\cos\beta}\right) = 17.5\,\mu\cdot\left(\frac{\cos\beta_B}{\cos\beta}\right) \qquad 4.28$$

which has the extreme limits (in the 26th order) of 15.6 μ

and 20.0 μ, which are acceptable. For the projected slit height, on the other hand, the anamorphic magnification factor ($\cos \alpha'/\cos \beta'$) differs from unity by less than 0.005 at its extreme limits. Therefore the slit height h corresponding to h' = 0.99 mm is

$$h = \frac{f_1}{f_2} h' = 1.44 \text{ mm} \quad . \qquad 4.29$$

Of course, the stellar spectrum will be widened to only $\frac{1}{2}$ mm (by trailing the star along the slit), and the outer portions of the slit will be blocked off. Conversely, when the comparison spectra are exposed, the central 0.72 mm of the slit will be blocked off. Substituting this value of h into equation 3.26, we find that when G = 1789 mm (see Figure 3.1), the diameter of the collimator mirror required to avoid vignetting is

$$d_1' = 51.76 \text{ mm} \quad . \qquad 4.30$$

Since the angle ξ subtended by the collimator at the near edge of the échelle must satisfy $\xi < 2\theta - (\Delta\beta)_{max} = 10.544°$ to avoid vignetting, this edge must be therefore at least $d_1'/\tan(10.544°) = 278.1$ mm distant from the échelle to avoid vignetting.

These data are all summarized by Figure 4.3, which shows the final arrangement of the collimator and diffraction gratings. Since the short and long wavelength range

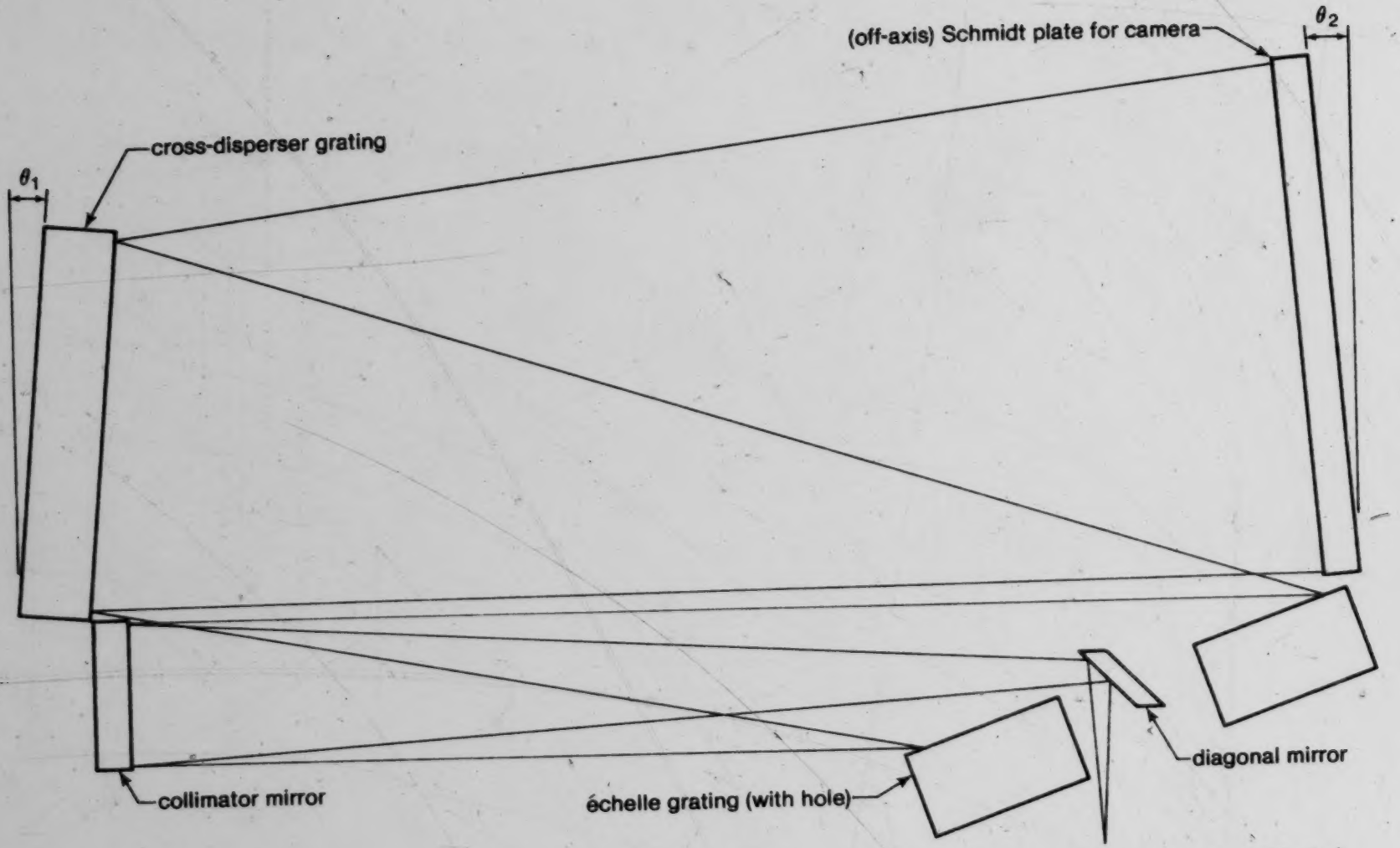

Figure 4.3(a): Side view of the spectrograph, drawn to one-half scale. Since $\gamma' = \gamma_o - (\beta - \beta_o)$ where $\gamma_o = 9°$, and $\theta = 7°$, the angles shown are $\theta_1 = (2\theta - \gamma_o) = 5°$ and $\theta_2 = 2(\gamma_o - \theta) = 4°$. The rays shown are for the extreme values of β, which occur in the long wavelength range.

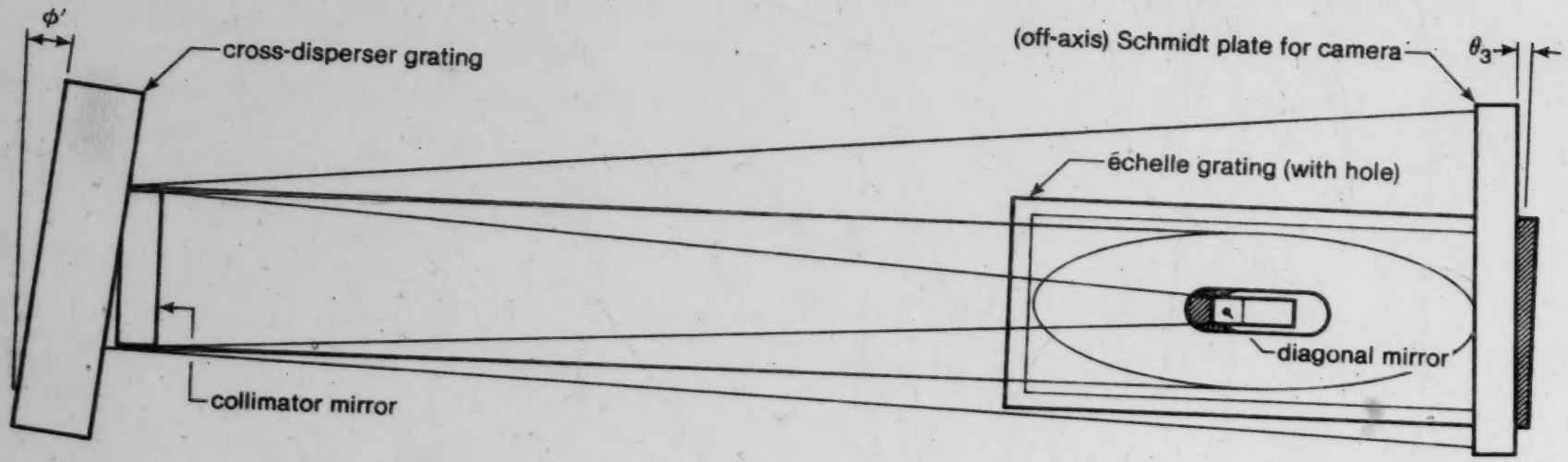

Figure 4.3(b): Top view of the spectrograph, drawn to one-half scale. Here, $\phi' = 6.892°$, for the short wavelength range. For the long wavelength range, $\phi' = 5.509°$. From Figures 4.1 and 4.2, $\theta_3 = 1°56'$. The rays shown are for the extreme values of β', which occur in the short wavelength range. Spread in the collimated beam is due to $h = 1.44$ mm > 0.

configurations differ only in the angle of incidence of the cross-disperser grating, by 6.892°-5.509° = 1.383°, the same diagram serves for both.

It remains to calculate the spectrograph's resolution, plate factor and an (optimistic) estimate of the throughput. Since these all vary with diffraction angle, we calculate them for $\beta = \beta_B = 56.435°$, to give representative values. From equation 3.7 we find the resolution to be

$$R = \lambda/\delta\lambda = 50,500 \qquad 4.31$$

corresponding to $\delta\lambda = 0.1$ Å at $\lambda = 5000$ Å. (From equation 3.8, we easily compute that $R/R_o \leq 0.1$ at $\lambda = 5000$ Å, in agreement with our earlier comments.) From equation 3.13, we find the plate factor (reciprocal linear dispersion) to be

$$P = 1.13\ (\lambda/1000\ \text{mm}) \qquad 4.32$$

or 5.65 Å/mm at $\lambda = 5000$ Å. In order to estimate the throughput L from equation 3.9, we need to first estimate the overall spectrograph transmittance, τ_o, which is the product at all the surface reflectances and grating efficiencies. The échelle efficiency is $(\frac{\cos\alpha}{\cos\beta_B}) \approx 0.60$, the cross-disperser efficiency is $(\frac{\cos\alpha'}{\cos\beta_B}) = 1.00$, while there are six aluminized surfaces (2 collimator, 2 grating, 2 camera (assumed)), each of reflectance ≈ 0.88, hence

$$\tau_o \simeq 0.6\ (0.88)^6 = 0.28\ . \qquad 4.33$$

Hence, taking $\Psi' = w/F = 2.0"$ arc $= 9.7 \times 10^{-6}$ radian, and Ψ as the angular diameter of the seeing disc, i.e. $\Psi \simeq$ 3" arc $= 14.5 \times 10^{-6}$ radian, we find, since D = 50.8 cm, that

$$L \simeq 8 \times 10^{-8}\ \text{steradian} \cdot \text{cm}^2\ . \qquad 4.34$$

Of course, the actual throughput will probably be nearer half this figure, but this estimate will be used later to compute the magnitude reach of the spectrograph.

We now need to design a suitable camera for this spectrograph, which we do in the next chapter.

CHAPTER 5

CAMERA DESIGN

As mentioned previously, in chapter four, our camera design is practically dictated by the aperture, focal length, and field coverage required by the spectrograph design. From Figure 5.1 the aperture must be ~110 × 180 mm (a rectangle with one round edge), while the focal length is only 275 mm, and the aberrations must be kept small over a field of 40 mm or ~8.3°. Thus our camera must be anastigmatic, which in turn requires a catadioptric design employing a full-aperture correcting lens or plate.

Since the 40 mm diameter minimum central obstruction needed to make the image accessible would vignette around 40% of the ~50 × 83 mm beam, we must use an off-axis design, which will therefore be, in effect, half of an ~f/1 or faster camera. Thus our choices are narrowed down to a field-flattened Schmidt camera or a Baker camera. The former employs a plano-convex lens just inside the focus to flatten the field, while the latter uses a Cassegrain-type secondary mirror to the same effect.

If a Schmidt camera is folded with a plane mirror, the focus becomes accessible, with a minimum central obstruction, and only one aspherical surface need be made. On the other hand, a Baker camera, although it has smaller aberrations than the field-flattened Schmidt (for the same

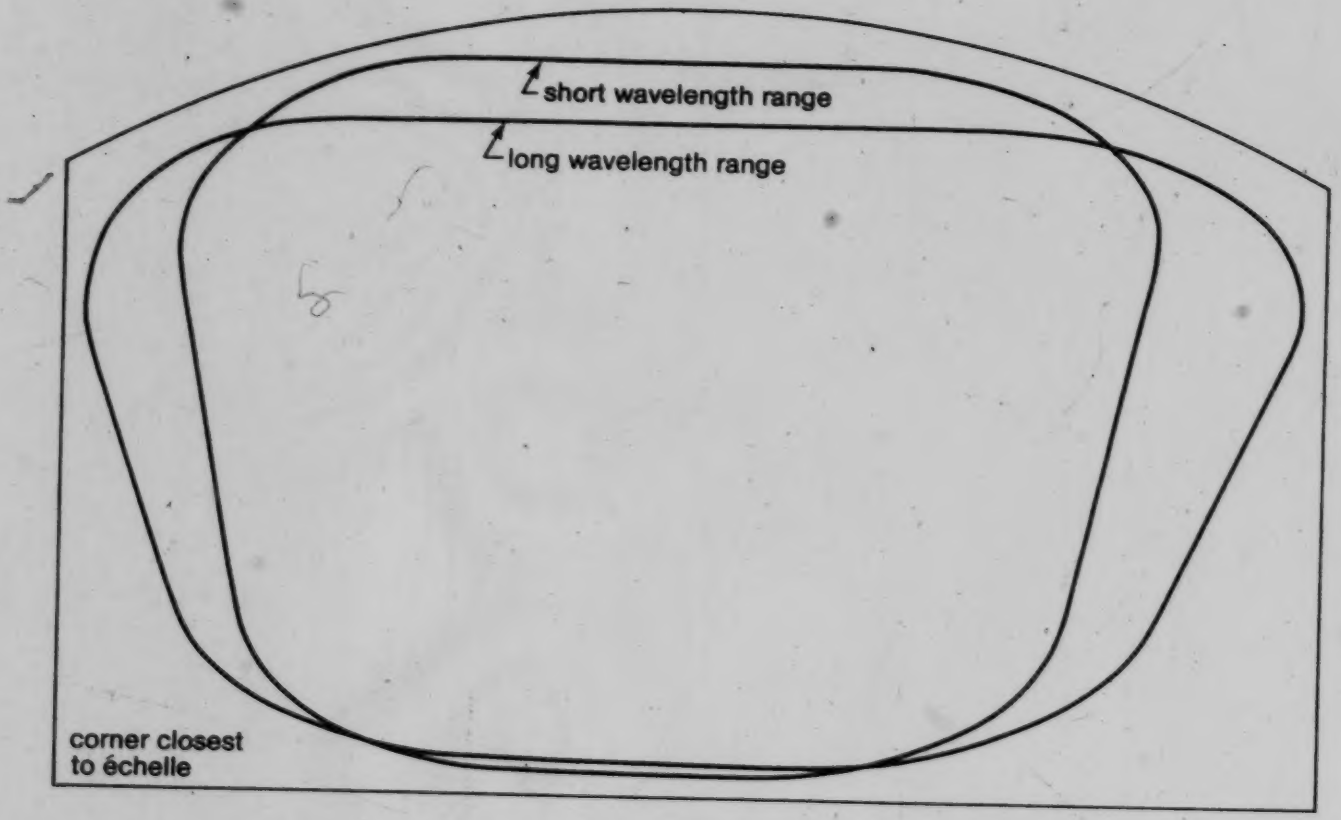

Figure 5.1: Illumination pattern of camera corrector plate, drawn to full scale. Two ~115 × 185 mm plates are cut from a 381 mm (15 inch) diameter UBK-7 blank, one each for the blue (3383-5537 Å) and red (5299-8795 Å) cameras, and appropriately multicoated to reduce scattered light.

aperture), requires a large secondary ($q \gtrsim 0.4$) to make the image accessible, and thus much larger optics must be employed to obtain the same off-axis aperture. Also, at least one of the mirrors must be made aspheric, in addition to the corrector. (A variation, due to Linfoot, keeps both mirrors spherical, but requires a second aspheric corrector, which then, however, allows apochromatism, as well as anastigmatism, by arranging that the two correcting plates have compensating colour errors.) For these reasons, we choose to use an off-axis folded Schmidt camera, with a field-flattening lens.

Since we are using an off-axis design, it requires little more work (an extra field-flattener) to make a second camera at the same time. This allows each camera to be multi-coated for one of the two wavelength ranges, thus reducing scattered light, and the field-flattening lenses can then be individually optimized, as well.

From Figure 4.1 we see that the 'blue' camera will cover the range 3383-5537 Å and, similarly, from Figure 4.2, the 'red' camera has a range 5299-8795 Å (with a gap from 5406-5416 Å, due to the 'missing' parts of orders 41 and 42). Thus, for the red camera, in order to eliminate the second order of the cross-disperser grating, we need a filter with essentially zero internal transmittance shortward of 8795 Å/2 ≈ 4400 Å, but good internal transmittance longward of 5300 Å. These requirements are met

by Schott glass type GG 475. For a 3 mm thickness, at 20°C, the internal transmittance varies from $<10^{-5}$ to >0.99 over the range 4500-5250 Å. At -35°C, this range shifts to about 4450-5200 Å (Melles Griot Optics Guide, 1975). In order to avoid introducing any aberrations or focal shifts, the (plane-parallel, multi-coated) filter should be placed immediately in front of the corrector plate of the red camera.

Preliminary Design[†]

The Schmidt camera consists of a spherical mirror with an aspheric corrector plate at its center of curvature. Now a spherical mirror with its aperture stop at the center of curvature has no aberrations except spherical aberration (which, unfortunately, is ruinous to the definition for apertures greater than ~f/10) and field curvature, the spherical focal surface being concentric with the mirror. By introducing a figured plate at the center of curvature, the spherical aberration is corrected, and the field is then limited by the higher-order aberrations of the plate, for oblique rays. Since spherical aberration and coma are now both zero, these and the astigmatism are now independent of the entrance pupil position. Since the astigmatism vanishes, the curvature (reciprocal radius of curvature) c_o of the focal surface is given by the Petzval sum

---

[†]For this section, we refer to the Handbook of Optics (1978).

$$c_o = \sum_i \left(\frac{n_i - 1}{n_i}\right) c_i \qquad 5.1$$

where $c_i = 1/r_i$ is the curvature of the ith element, of index of refraction n_i. The sign of the curvatures is chosen so that the power (reciprocal focal length) $(n_i - 1)\, c_i$ of a converging element is positive. Note that $n = -1$ for mirrors. For a plano lens, the magnitude of r_i is the radius of the curved side. For an aspheric surface, r_i is the 'paraxial' radius of curvature, i.e. the radius of the sphere tangent to the surface at the optical axis. An aspheric of 'strength' b therefore has a surface equation

$$x = \frac{y^2}{2r_i} + \left(\frac{1 - b}{8r_i^3}\right) y^4 + \ldots \qquad 5.2$$

where x is the depth of the surface at radius y from the optical axis. For a conic of eccentricity e, $b = e^2$.

From aberration theory, the first (outer) surface of the Schmidt plate should be plane, while the second requires the profile

$$x = \frac{y^4}{4(n_1 - 1)\, r_2^3} \qquad 5.3$$

where r_2 is the radius of curvature of the mirror, and the surface is curved so that the plate is thicker at the edges, and thus the Schmidt plate cannot correct field curvature. In practice, however, the chromatic aberration introduced by such a plate is reduced by adding a small

opposing r^2 term, so that the plate as a whole is more nearly flat. The extra aberrations so introduced are then eliminated by shifting the position of the plate slightly. From the Handbook of Optics (1978), a very close approximation to the aspheric which will correct the spherical aberration and minimize chromatic effects is

$$x = \frac{1}{4(n_1 - 1)\, r_2^3}\left[-\frac{3}{2}\, y_m^2 y^2 + \left(1 - \frac{3}{4}\left(\frac{y_m}{r_2}\right)^2\right)^2 y^4\right] \qquad 5.4$$

where y_m is the maximum value of y. Thus the curvature c_1 of the plate is positive (since that of the mirror is negative), and in the amount

$$c_1 = -\frac{3}{8(n_1 - 1)}\left(\frac{y_m}{r_2}\right)^2 c_2 \qquad 5.5$$

or less than 6% of the mirror curvature $c_2 = 1/r_2$ for an f/0.9 camera ($y_m = r_2/3.6$), assuming $n_1 \geq 1.5$. Since this changes the field curvature c_o by <1%, we must introduce a field-flattening lens to make $c_o = 0$.

To reduce the aberrations of the field-flattening lens to a minimum, we place it as near the focus as possible, next to the image-tube entrance window, and make the adjacent surface plane, so that its aberrations will be negligible. Then the flat-field condition $c_o = 0$ and equation 5.5 give the curvature c_3 of the field-flattening lens as

$$c_3 = \left(\frac{n_3}{n_3 - 1}\right)\left(\frac{3}{8n_1}\left(\frac{y_m}{r_2}\right)^2 - 2\right) c_2 \qquad 5.6$$

which will be positive. Considering now the lens plus window as the field-flattener, of (combined) edge thickness t_o at semidiameter y_o, we find, using equations 5.2 and 5.6, that the effective center thickness is approximately

$$t \simeq t_o - \left(\frac{n_3}{n_3 - 1}\right) \frac{y_o^2}{r_2} \quad . \qquad 5.7$$

We set the lens edge thickness at 1.00 mm and y_o to avoid vignetting. The effective focal length of the camera can then be found to be, from Gaussian (first-order) optics,

$$f_2 = -\frac{r_2}{2} \frac{\left(1 - \left(\frac{n_3 - 1}{n_3}\right) \frac{t}{r_3}\right)}{\left(1 + \left(\frac{n_3 - 1}{2}\right) \frac{r_2}{r_1}\right)}$$

$$\simeq -\frac{r_2}{2} \frac{\left(1 + 2\frac{t_o}{r_2} - \left(\frac{2n_3}{n_3 - 1}\right)\left(\frac{y_o}{r_2}\right)^2\right)}{\left(1 - \frac{3}{16}\left(\frac{y_m}{r_2}\right)^2\right)} \qquad 5.8$$

the numerator and denominator representing the effective magnifications of the field-flattening lens and corrector plate, respectively.

Thus, we need to first estimate y_m before proceeding further. In Figure 5.1, we have set the closest edge of the aperture 76 mm (3 inches) away from the optical axis to avoid the vignetting of the beam which would otherwise be caused by the image-tube assembly (see Figure 5.3). This means that the corrector plate must be 381 mm (15 inches) in diameter. Allowing for a 1 mm wide chamfer around the

edge, we therefore set $y_m = 189$ mm. Since the folding flat must be at least 40 mm larger in each dimension than the corrector aperture, we find that we need a 318 mm (12.5 inch) diameter blank to make two such flats, as shown in Figure 5.2(a). This size also allows for about a 6½% increase in the required shorter dimension of the flats, due to the oblique incidence of the beam from the corrector, as shown in Figure 5.3(b). Since the mirror must again be at least 40 mm larger in each dimension than the flat, we find we need a 406 mm (16 inch) diameter blank to provide two mirrors, as shown in Figure 5.2(b). Since the mirror is spherical, the central sections can be regarded as off-axis sections merely by shifting them tangentially to their surfaces.

The remaining parameters are chosen as $y_o = 23$ mm, $t_o = 6.10$ mm, $n_1 = n_3 = 1.5228$ (for UBK-7) and $f_2 = 275.00$ mm. Equation 5.8 is then iterated twice to yield the required value of $r_2 = -555.82$ mm. Hence, from equation 5.4, the required corrector profile is, for x and y in millimeters:

$$x = 1.4922 \times 10^{-4} y^2 - 2.3228 \times 10^{-9} y^4 \qquad 5.9$$

The 'neutral zone' of the corrector, where it is plane-parallel ($dx/dy = 0$), and has its maximum figuring depth, is therefore at $y = 179.2$ mm, corresponding to $x = 2.397$ mm. From equation 5.6, the radius of curvature of the convex side of the field-flattening lens is

$$r_3 = \frac{1}{c_3} = 96.79 \text{ mm} \qquad 5.10$$

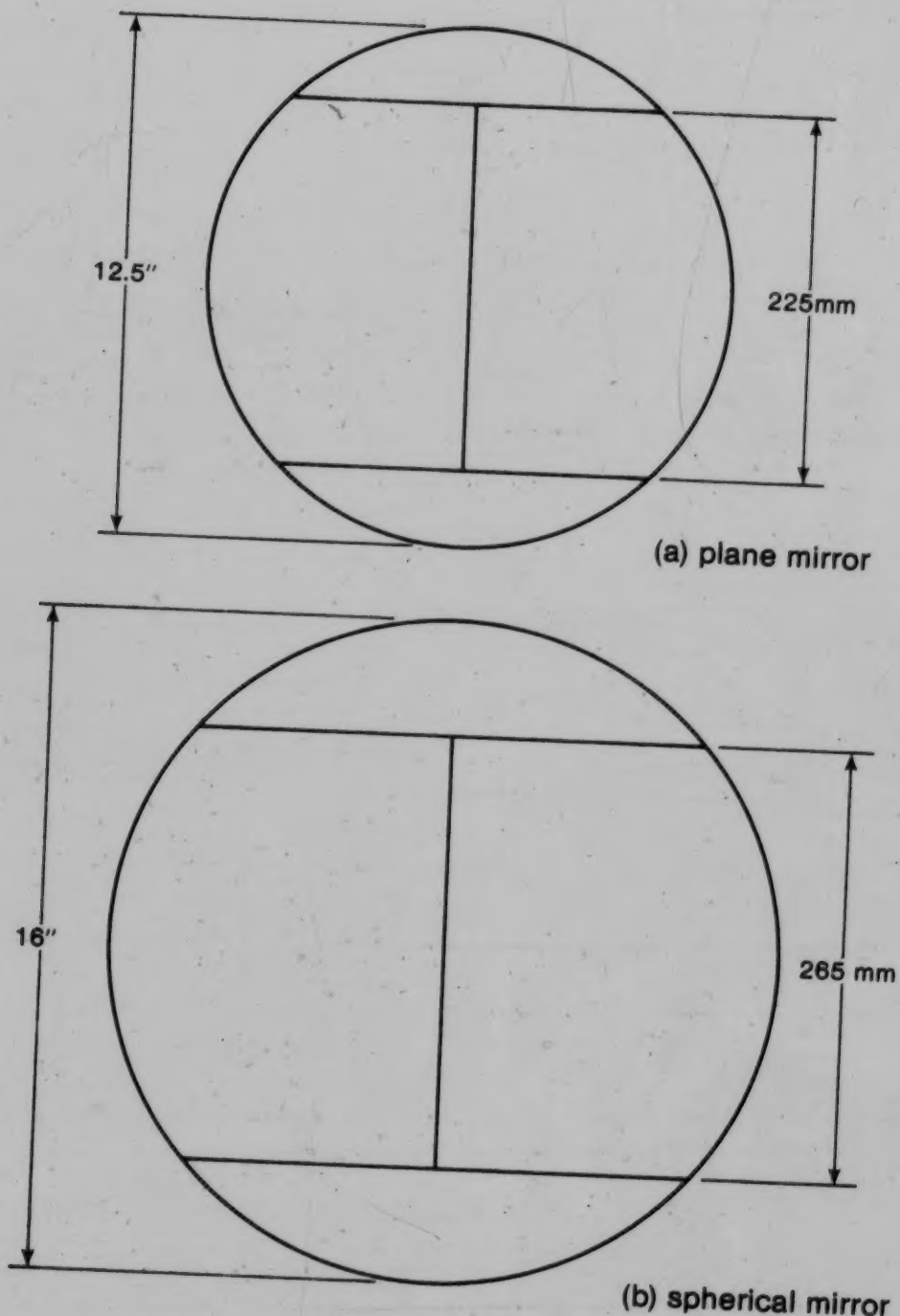

Figure 5.2: Sectioning of the plane mirror to provide two folding flats, and of the spherical mirror to provide two 'off-axis' camera mirrors, drawn to one-quarter scale.

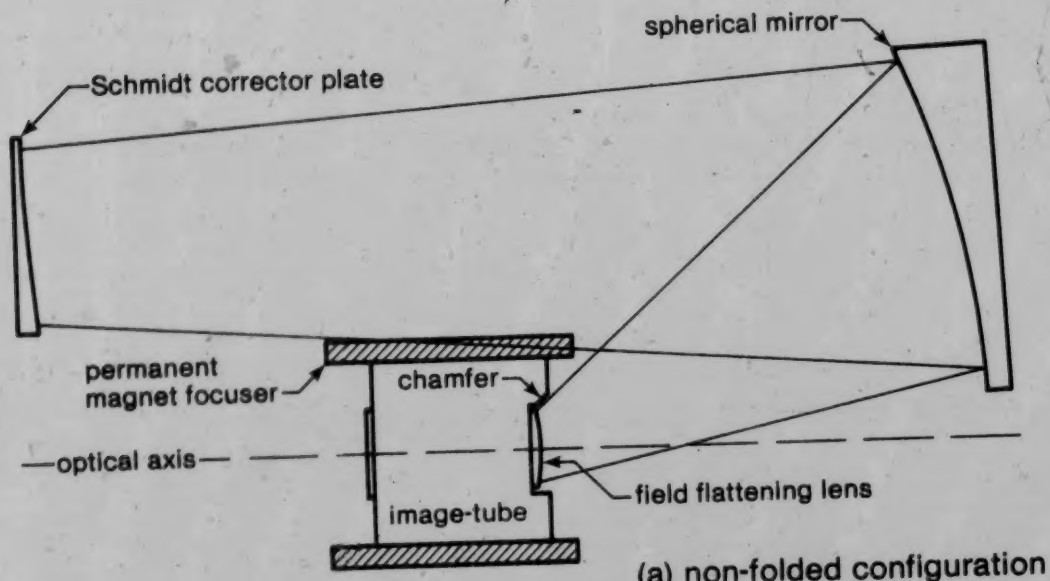

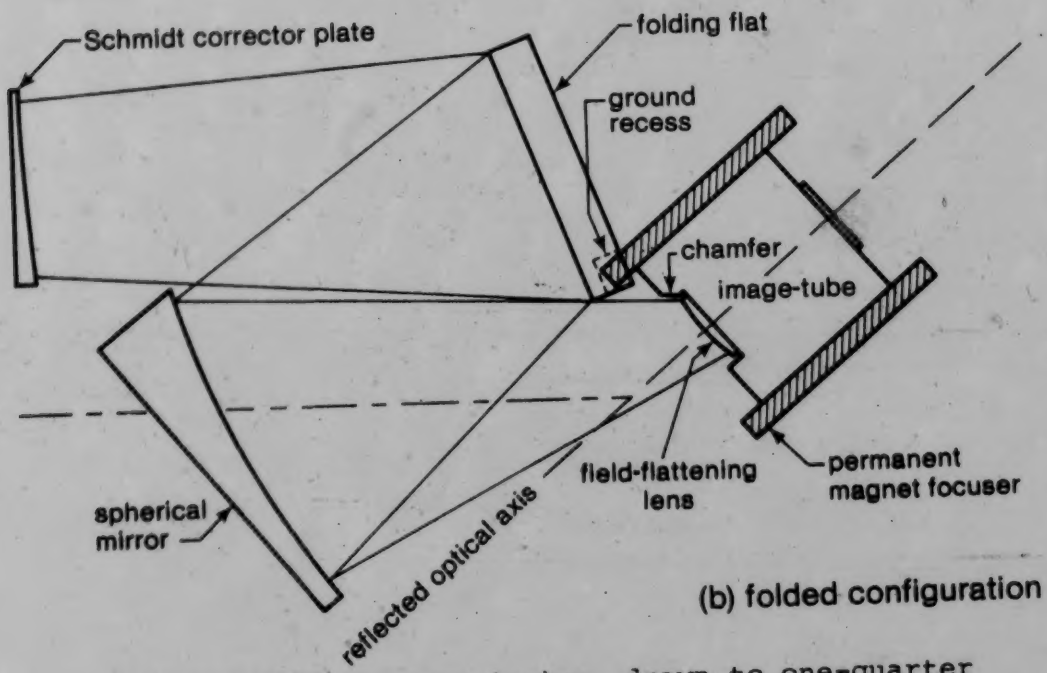

Figure 5.3: Prelimary camera design, drawn to one-quarter scale. (Depth of Schmidt plate shown full scale for clarity). Image-tube shown is ITT F-4089 (see chapter six). Vigetting loss in configuration (a) is ≤4%. Note chamfer required in image-tube plotting compound, and ground recess required in folding flat for configuration (b). Round edges of all elements are towards top of page.

and hence, using equation 5.2 (with b = 0), its central thickness is, for $t_o = 6.10$ mm and $y_o = 23$ mm,

$$t = t_o + y_o^2/2r_3 + y_o^4/8r_3^3 = 8.87 \text{ mm} . \qquad 5.11$$

The field-flattener is found, from Gaussian (first-order) optics, to be separated from the camera by a distance

$$s = \left|\frac{r_2}{2}\right| \frac{(1 + (n_1 - 1)\frac{r_2}{r_1})}{(1 + \frac{1}{2}(n_1 - 1)\frac{r_2}{r_1})} - \frac{t}{n_3 - (n_3 - 1)\frac{t}{r_3}}$$

$$\sim \left|\frac{r_2}{2}\right| \frac{(1 - \frac{3}{8}(\frac{y_m}{r_2})^2)}{(1 - \frac{3}{16}(\frac{y_m}{r_2})^2)} - \frac{t}{n_3} = 265.92 \text{ mm} . \qquad 5.12$$

Since the corrector plate is a distance $|r_2|$ from the mirror, this completes the preliminary design. The final computer-optimized design will not differ substantially from this preliminary design, and hence the final arrangement of the camera optics will essentially be given by Figure 5.3. Here, we see that since the camera operates at such a large distance off axis, it need not be folded to make the image accessible. Although there is some vignetting in the non-folded configuration, it only amounts to $\lesssim 4\%$, comparable to the light loss from a multi-coated mirror. Since the non-folded configuration is inherently less susceptible to suffering from scattered light in the image plane, and saves making a large optical flat, we recommend it as being superior to the folded configuration initially chosen.

Final Design

For the final optimization of the camera parameters, a computer is used to optimize the geometrical blur-spot sizes over the required field, which are obtained by tracing a large number of rays through the system, numerically. Such an optimization procedure has been applied to the preliminary design by Dr. Harvey Richardson of the Dominion Astrophysical Observatory, leading to the following results:

Although the spherical aberration and Seidel (third order) aberrations of coma, astigmatism and field curvature are well corrected in the preliminary design, higher order coma and astigmatism become large near the edges of the field. By balancing these against controlled amounts of the Seidel aberrations, the maximum blur-spot sizes can be reduced by a factor of about three, but the camera resolution remains aberration-limited at the ends of the extreme orders in each wavelength range. Normally, the higher-order aberrations of the Schmidt camera are small, since placing the entrance pupil coincident with the corrector plate, at the center of curvature of the mirror, minimizes higher-order coma and eliminates the astigmatism of the mirror for all orders. Also, these aberrations vary inversely as the third and higher powers of the off-axis focal ratio; hence the low off-axis focal ratio of the camera (~ f/0.75) allows them to be brought into prominence here by the removal of the entrance pupils at the cross-

disperser and échelle gratings from the center of curvature (by about 1.5 f_2 and 2.9 f_2, respectively).

Thus Dr. Richardson suggests replacing the reflection cross-disperser gratings by the equivalent transmission gratings, allowing the Schmidt camera to immediately follow in the optical train. Then the cross-disperser entrance pupil would be near the center of curvature of the camera mirror and the distance to the échelle entrance pupil would be halved. This would also halve the required off-axis aperture, and allow a smaller correcting plate to be used, with no vignetting from the image-tube assembly. The combination of the increased focal ratio and reduced separation of the entrance pupils from the center of curvature results in an order of magnitude improvement in the images. A preliminary design, based on a 12 inch (305 mm) diameter corrector, yields images $\lesssim 25\,\mu$ across over an 8° field. (Aside from the smaller aperture of the Schmidt plate, the design remains substantially unaltered from Figure 5.3(a).)

The only change in the spectrograph parameters is in the constant γ_o (see Figure 4.3(a)), which defines the tilt of the cross-disperser grating with respect to the incident beam from the échelle. Using a transmission cross-disperser grating allows $\gamma_o = 0°$, which results in a slight reduction in the angular separations of the échelle orders. This in turn allows the camera focal length to be increased, by a couple of percent, so that the minimum linear échelle

order separation (at m = 66) actually improves, along with the reciprocal linear dispersion (plate factor). Of course, the red and blue camera positions may be different, but interchangeable mountings will be constructed and individually permanently aligned, in any case.

As a result of these changes, the final spectrograph design, using the transmission gratings, will be published later in a joint paper with Dr. Richardson.

CHAPTER 6

DETECTOR SELECTION

Basically, our spectrograph has been designed to operate photographically, with an image-tube. Although several purely electronic devices have recently become available, they do not yet offer the simplicity, economy and permanence of record of the photographic process, and hence we relegate their use to an interesting possibility for the future. Thus, the purpose of this chapter will be to select the most suitable photographic emulsion(s) and image-tube.

Plate Selection

Because of the superior dimensional stability, flatness and rigidity of glass over film, we will choose to use photographic plates instead of film. Since the spectroscopic study of faint objects requires long exposures, we will restrict ourselves to the use of Kodak spectroscopic plates, in order to minimize the amount of the reciprocity failure of the emulsion (see next paragraph). Because these plates also offer the highest available resolution and long-exposure sensitivity, they are standard for spectroscopic use, and thus also facilitate comparisons of instrumental performance and observational results.

The (total) exposure of a photographic plate is defined as the product of the irradiance and the exposure

time (which is also often called, simply, 'the exposure'). The sensitivity of an emulsion is defined as the reciprocal of the exposure (in erg/cm^2) required to produce a stated density of the image above the background (gross) fog. Ideally, the sensitivity of an emulsion should be independent of wavelength (at least over a certain range) and irradiation level. The actual variation of the sensitivity with wavelength is called the spectral sensitivity, and the variation with irradiance is called the reciprocity curve. Decreasing sensitivity of the emulsion for fainter irradiation levels is called 'reciprocity failure', because then the required exposure (time) is greater than that indicated by the reciprocal of the irradiance.

For faint astronomical sources, the random scatter in photon arrival times, and, in the case of image-tube detection, thermionic emission from the photocathode, become significant and reduce the incoming signal-to-noise ratio to low levels. In this case, to optimize the signal-to-noise level of the image, the optimum level of exposure is about 0.6 to 1.0 density above gross fog, depending on the emulsion (Kodak 1973). Also, for practical reasons, exposure times must be kept reasonable. Thus, in Figure 6.1, we show the approximate spectral sensitivity of selected Kodak spectroscopic plates for a density of 0.6 above background (gross) fog and a one hour exposure, and indicate the (slight) changes for half-hour and two hour exposures.

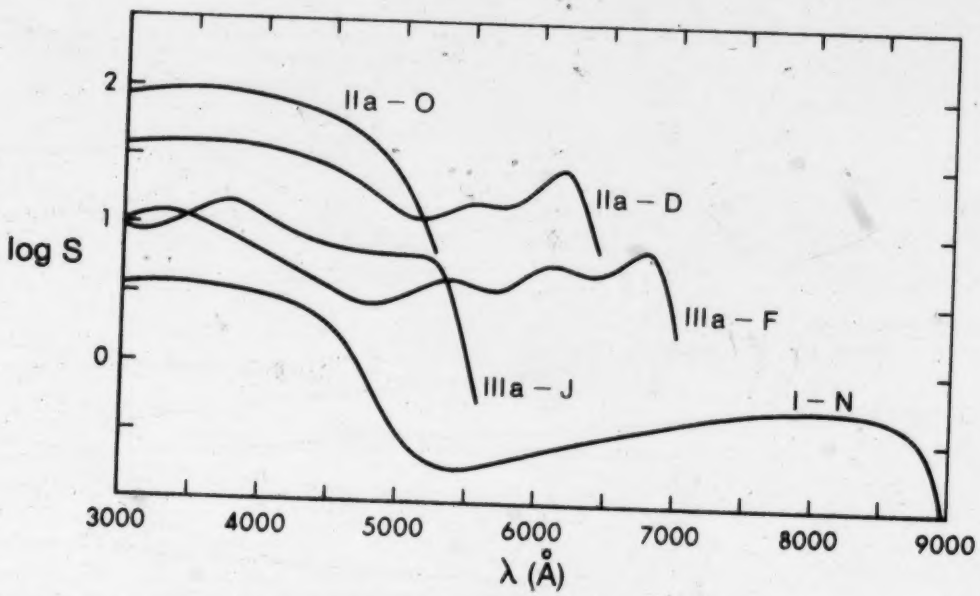

Figure 6.1: Approximate spectral sensitivites of Kodak spectroscopic plates, for a one-hour exposure. Sensitivity equals reciprocal exposure (in erg/cm^2) required to provide a density of 0.6 above gross fog. Log S increases (decreases) by ~0.13 for a half-hour (two hour) exposure for I-N, IIa-O and IIa-D, and by ~0.09 for IIIa-J and IIIa-F. Curves derived from data published by Kodak (1973, 1976) and Cromwell and Dyvig (1973).

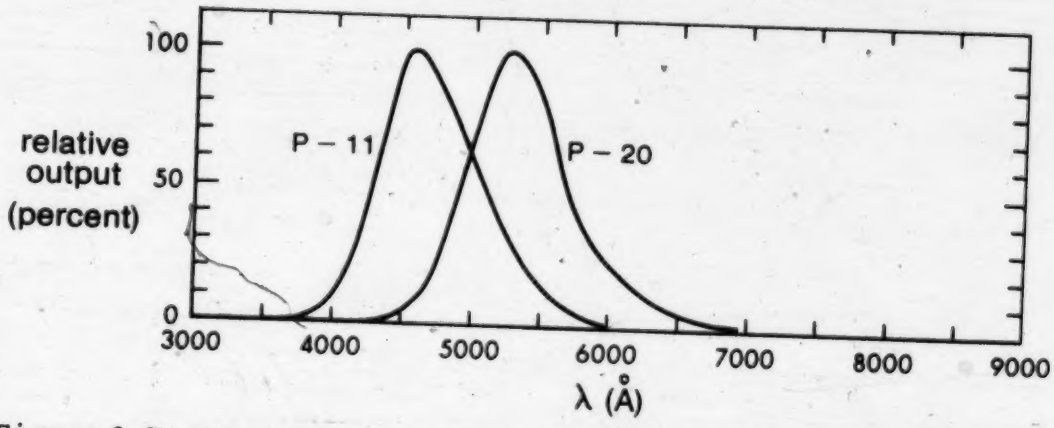

Figure 6.2: Spectral energy distribution of P-11 and P-20 phosphor screens. P-11 data from Cromwell and Dyvig (1973), P-20 data from material published by ITT (1974).

The IIIa emulsions offer about twice the resolution of the IIa and I-N emulsions.

For Direct Exposures

Since all the emulsions of Figure 6.1 have sufficient resolution (which is why Ia emulsions are excluded), the factors to consider in selecting a suitable emulsion are speed (sensitivity) and spectral response. For the 'blue' range, 3383-5537 Å, the best choice is clearly IIa-D. For the 'red' range, 5299-8795 Å, the only choice is I-N. In practice, the poor sensitivity of the I-N plate is overcome by 'hypersensitizing' it immediately before exposure (e.g. by bathing it in a 10^{-3}-10^{-4} molar silver nitrate solution). This results in a sensitivity (speed) roughly comparable to that of (untreated) IIa-D. Of course, IIa-D can also be hypersensitized (e.g. by soaking in dry hydrogen), but in this case the gains in sensitivity are much less spectacular (a few times). We remark that, in general, hypersensitizing results in plates which have an increased background fog density (by typically ~0.1) and hence a reduced signal-to-noise ratio, over equally dense untreated plates, but which require only a fraction of the exposure. (See Kodak publication P7-670 (1979) for further references.)

For Image-Tube Exposures

Here, we must again consider the factors of speed and spectral response, but now we must match the spectral

response of the emulsion to the spectral energy distribution of the phosphor screen of the image-tube. This distribution is shown in Figure 6.2 for the standard alternatives of P-11 (blue) and P-20 (green) phosphors. Comparing Figures 6.1 and 6.2, it is clear that the best emulsion-phosphor combinations are IIa-0 with the P-11 phosphor and IIa-D with the P-20 phosphor. From the results of Cromwell and Dyvig (1973), we find that these two combinations are, in fact, equally fast (sensitive). However, since the IIa-0 and IIa-D emulsions have essentially identical resolutions, while the grain size of the crystals in the P-20 phosphor is only about half that in the P-11 phosphor, it is obvious that the best combination is the IIa-D plate and P-20 phosphor screen, which we accordingly select.

Image-Tube Selection

Image-tubes are image intensification devices which increase the effective speed of the spectrograph by a factor of about 80 times (gain in radiant power for a 'single stage' image-tube), with little attendant reduction of the signal-to-noise ratio. The tube mechanism is as follows: The image formed by the spectrograph is incident, through an input window, onto a photocathode, which contains alkali metals such as cesium, sodium or potassium. Incident photons release photoelectrons via the photoelectric effect; the number of photoelectrons per photon is called the quantum efficiency of the photocathode, which is related to its sensitivity.

These photoelectrons are then (noiselessly) accelerated (in vacuo) through a large potential (typically 15 kV) and either electrostatically or magnetically focused onto a phosphor screen, which reproduces an intensified version of the original image, in a similar manner to a television screen. The image is then fiber-optically transferred onto the emulsion, if the tube is a single stage type being used for contact photography, or onto another photocathode, for a multiple stage tube. The output phosphor screen is usually aluminized on its internal surface to prevent externally incident light from reaching the photocathode, and contaminating the image. This thin aluminum film is completely transparent to the energetic photoelectrons. Image-tubes are described by their useful photocathode diameter, number of stages, type of focusing, photocathode spectral response and phosphor screen type. The primary criteria for selecting an image-tube are high resolution, uniform response and low background noise.

In their "Laboratory Evaluation of Eleven Image Intensifiers", Cromwell and Dyvig (1973) find that the limiting photographic resolution, R_p, is reduced from the limiting image-tube resolution, R_T. The relationship depends on the emulsion, and whether contact photography or a transfer lens is used, but is nearly independent of tube type. For contact photography, an analysis of their graphs shows

$$R_P \simeq 6\ R_T^{0.33} \quad \text{(IIa emulsions)} \qquad 6.1$$

$$R_P \simeq 6\ R_T^{0.38} \quad \text{(IIIa emulsions)} \qquad 6.2$$

for R_P and R_T in lp/mm (1000/resolution in μ) and for 50 lp/mm < R_T < 100 lp/mm. This range corresponds to about 21.8 lp/mm < R_P < 27.4 lp/mm for IIa emulsions, and about 26.5 lp/mm < R_P < 34.5 lp/mm for IIIa emulsions. This loss of resolution can be attributed, in part, to the lack of close contact between the fiber-optic faceplate and the photographic plates, due to the non-flatness of the latter. For this reason, 'selected flat' plates should be ordered. Also, Cromwell and Dyvig (1973) recommend using a foam rubber pad and pressure plate arrangement as providing the most reliably uniform contact. The remaining loss of resolution is probably due to image-spread in the emulsion, which is still a poorly understood phenomenon. Although slightly higher photographic resolution can be obtained by using a transfer lens, the low efficiency (≲ 5%) of this method precludes its use here. Thus, to obtain the maximum resolution on the plate, the image-tube should be selected to give maximum resolution, as well.

Now, the intrinsic resolutions of the photocathode and phosphor screen are very high (~ 200 lp/mm), hence the resolution of the image-tube depends on the number of fiber-optic elements and the focusing aberrations. Since electrostatically focused tubes require strongly curved

photocathodes, their input windows must be fiber-optic for any appreciable aperture. Besides degrading the resolution, standard fiber-optic materials have poor transmittance below 4000 Å, and alternate materials only transmit above 3500 Å. Since the inner surface of the fiber-optic output plate must also be strongly curved, to match the field curvature of the electrostatic lens, electrostatic image-tubes also suffer from a strong radial dependence of sensitivity. This is due to the fact that the phosphor, deposited on the curved surface, is a Lambertian emitter (i.e. radiates uniformly in all outward directions). According to Dr. Stanley Jeffers of York University (private communication), the relative decrease in sensitivity from the center to the edge of the field can amount to 3 magnitudes (16 times). Also, electrostatically focused image-tubes have background noise levels an order of magnitude greater than magnetically focused image-tubes, for the same photocathode sensitivity. At Dominion Astrophysical Observatory, Mr. Chris Morbey reports that, for these reasons, not a single paper has resulted from work done with their electrostatic image-tubes (private communication). On the other hand, magnetically focused image-tubes offer high resolution, low distortion, uniform response, and background noise levels determined solely by thermally generated electrons from the photocathode (thermionic emission), which can therefore be reduced by cooling (typically by one order of magnitude per 15°C). For these reasons, we choose to use a magnetically focused image-tube,

even though they are about twice as expensive as comparable electrostatic types.

If the magnetic focusing field were uniform and had no radial component, the image-tube would have no aberrations whatsoever. Since the solenoidal focusing coils normally used to generate this field closely approximates this condition, the aberrations are small. However, the liquid cooling required by these solenoids is highly impractical during Alberta winters, so we will use instead a permanent magnet focuser, and accept the slight reduction in R_T which results.

Of the currently available image-tubes, ITT's magnetically focused image-tubes have about 50% higher resolution than any competitors, and their 40 mm diameter tubes F-4089 (single stage) and F-4091 (two stage) can be supplied with permanent magnet focusers. It is important to note that the magnetization of each focuser is individually adjusted to optimize the performance of its image-tube. Since the single-stage tube has much higher resolution and lower cost, we will use an ITT F-4089 image-tube with a permanent magnet focuser. Since we have already elected to use the (standard) P-20 phosphor screen, it remains to choose the input window material and photocathode spectral response. In order to assure good ultraviolet transmittance, we will choose a quartz (fused silica) input window. This is a standard option. Of the available photocathodes, S-20/S-25 multialkali types MA-2, MA-3 and MA-4 offer progressively better

infrared response (e.g. at 8800 Å), and progressively worse ultraviolet response (e.g. at 3400 Å). Since the slight fall-off of the MA-3 response at shorter wavelengths is compensated for by the increased blaze efficiency there, compared to middle wavelengths (see Figure 4.1), while its red response is only slightly inferior to that of MA-4, we select the MA-3 spectral response as the optimum choice for our photocathode. This completes the specification of our image-tube, and we accordingly summarize its characteristics below, in Table 6.1:

Photocathode to Anode Voltage	15 kV
Maximum Ambient Temperature	
Non-Operating	55°C
Operating	45°C
Photocathode Sensitivity	
Radiant†	0.06 A/watt
Luminous††	180 μA/lm
Gain	
Radiant Power†	50-100 watts/watt
Luminous Flux††	65-125 ft L./ft C.
Equivalent Background Input (23°C)	
Radiant†	$< 3 \times 10^{-14}$ watt/cm^2
Luminous††	$< 8 \times 10^{-12}$ lm/cm^2
Resolution (In Permanent Magnet)	
Center	80 lp/mm
Edge*	70 lp/mm
Distortion	
Spiral	< 0.05 mm
Linear	< 0.5 %

Table 6.1: Characteristics of ITT F-4089 magnetically focused image-tube, which has unit magnification, with an MA-3 photocathode and P-20 phosphor screen. The background, strictly due to thermionic emission, is ~10^{-15}A/cm^2 at 23°C, and decreases by ~10^{-1} per 15°C cooler.
* The minimum edge resolution is 65 lp/mm.
† At wavelength of peak response (~5500 Å).
†† Luminous flux input from a standard 2854°K lamp.

CHAPTER 7

MISCELLANEA

In this chapter, we cover those aspects of the spectrograph design which do not fall under any of the previous headings.

Comparison Source Selection

As noted by Breckinridge, Pierce and Stoll (1975), recent developments in astronomical spectrographs, particularly échelle instruments, have resulted in a "need for a comparison source richer in lines than the well-known iron-neon spectrum in use for many years". They continue:

> The spectrum of the element thorium is particularly suited to this purpose: it is rich in lines. The element has[only one]natural isotope and hence no isotope broadening of lines; and the Z of the nucleus is even, hence the lines do not have hyperfine structure. The heavy nucleus results in lines of small Doppler width. It is a rare earth, with many inner electron shell transitions in the energy range corresponding to a wavelength range 3000 Å to 10,000 Å.

They then list approximately 1850 thorium emission lines between 2720 and 8805 Å, with an internal accuracy of better than ±0.001 Å, thus calibrating the thorium spectrum as a standard comparison source. To properly identify the

wavelengths, a finding chart for each échelle order can be easily prepared from the photographic atlas of the thorium spectrum published by Junkes and Salpeter (1964), of which the University of Alberta Department of Physics already has a copy.

Thus we will use a thorium hollow-cathode spectral tube as our comparison source. The Handbook of Optics (1978) lists two such tubes suitable for this purpose: one from Westinghouse (WL23028, 1½ inch (3.8 cm) in diameter); and one from Jarrell-Ash (JA-45-590, 1 inch (2.5 cm) in diameter). Both have quartz windows and a neon gas fill. They require a power source of approximately 10 mA at 140 V (270 V to start). Thus these tubes are very compact and convenient to use.

Limiting Magnitude of the Spectrograph

Since the faintest magnitude observable with the spectrograph depends on many factors not amenable to computation, we will estimate the apparent photometric magnitude m_p of a star which will produce a density of 0.6 above gross fog on an untreated IIa-D plate for a one hour exposure, both with and without the F-4089 image-tube (see chapter six).

From Schneiderman and Karo (1976), the average irradiance from a star of apparent photometric magnitude m_p at the aperture of the telescope is

$$I = 3 \times 10^{-9} \Delta\lambda \; 10^{-0.4 \cdot m_p} \text{ erg/cm}^2\text{/sec} \qquad 7.1$$

where $\Delta\lambda$ is the bandwidth in Å. For a telescope of aperture D, focal length F and transmittance τ, producing a seeing disc of angular diameter Ψ, the resultant radiance of the telescopic image is (in erg/cm^2/sec/steradian)

$$I' = \frac{\tau D^2 I}{\frac{\pi}{4}(F\Psi)^2} = \frac{\tau I}{\frac{\pi}{4} f^2 \Psi^2} \qquad 7.2$$

where the focal ratio $f = F/D$, as before. Now, the throughput L of the spectrograph is defined as the ratio of the output luminous flux to the input luminance, which is identical to the ratio of the output radiant flux to the input radiance, since the conversion factors (luminous efficacy) cancel. Thus the radiant flux of the spectrograph image is LI', and the irradiance, or areal density of the flux, for a bandwidth $\Delta\lambda = \lambda/R$, where R is the resolution of the spectrograph, is

$$I'' = LI/w'h' \qquad 7.3$$

where w' is the projected slit width and h' is the projected slit height, over which the image of the star is trailed during the exposure. Hence m_p will be the apparent photometric magnitude of a star producing a density of 0.6 above gross fog for an exposure T = 1 hour, without an image-tube, provided

$$1/S = I'' T \qquad 7.4$$

where S is the sensitivity of the plate, from Figure 6.1. Solving equations 7.1 to 7.4 for m_p, we find

$$m_p = 2.5 \log[ST(\frac{k\lambda}{R}) \frac{\tau L}{\frac{\pi}{4} f^2 \psi^2 w' h'}] \qquad 7.5$$

where $k \simeq 3 \times 10^{-9}$ erg/cm^2/sec/Å. Since, from equations 3.6, 3.7 and 3.13, we have

$$\frac{\lambda}{Rw'} = P \qquad 7.6$$

where P is the plate factor, equation 7.5 can be written

$$m_p = 2.5 \log[ST \frac{k\tau LP}{\frac{\pi}{4} f^2 \psi^2 h'}] \ . \qquad 7.7$$

Setting T = 3600 sec, L = 8×10^{-8} steradian.cm^2 (from 4.34), P ≃ 5.65 Å/mm (see 4.32), τ = 0.65 (2 mirrors plus silhouetting by the secondary), f = 8, ψ ≃ 3"arc = 14.5×10^{-6} radian, h' = 0.49 mm, we find, for S in (erg/cm^2)$^{-1}$

$$m_p \simeq 2.5 \log S - 3.0 \ . \qquad 7.8$$

From Figure 6.1, this gives $m_p \simeq -0.2$ for IIa-D, at 5000 Å. A similar calculation gives $m_p \simeq +0.6$ for IIa-D at 4000 Å. Hypersensitizing the plates would gain one or two magnitudes. For an image-tube exposure, I" is increased by a factor of ~75 (radiant power gain), which is equivalent, from equation 7.4, to increasing S by the same factor, or adding 2.5 log 75 ≃ 4.7 to the right-hand side of equation 7.7, yielding

$$m_p \simeq 2.5 \log S + 1.7 \ . \qquad 7.9$$

Here we must take S at the wavelength corresponding to the peak of the P-20 phosphor screen output, or ~5300 Å. This yields $m_p \simeq 4.5$ for IIa-D. This is comparable to the performance of the instrument described by Burton (1977). For the two-stage F-4091 image-tube, which has a radiant power gain of ~3500, a similar procedure yields $m_p \simeq 8.7$, so such a tube should be considered as a future addition to the spectrograph. We remark that if we use equation 3.9 to expand L, then equation 7.7 becomes

$$m_p = 2.5 \log[ST \frac{k\tau\tau_o}{f^2} (\frac{\Psi'}{\Psi} \frac{D^2 P}{h'})] \qquad 7.10$$

and the expression in parentheses becomes identical to the 'speed' derived by Bowen (1952) for his case II ($\Psi' < \Psi$).

Practical Considerations

To maintain high rigidity with low weight, a box-like magnesium alloy casting should be used for the main spectrograph structure, with provision made to attach either the red or blue camera assemblies at the output end. The spectrograph elements can then be mounted on aluminum alloy angle-section cross braces mounted in the box, and adjustments made through various access ports. This arrangement is similar to that used by Burton (1977). Since the telescope structure and mounting are also almost entirely made from aluminum alloy, mu-metal shielding of

the image-tube will therefore be unnecessary.

Also as described by Burton (1977), slit jaws made from highly reflecting diamond-cut Alcoa aluminum alloy can be used to provide a wide field (~ 20') for star acquisition and guiding with a low-power XY-scanning microscope. The slit assembly should also include provision for reflecting light from the thorium comparison source or helium-neon alignment laser through the slit and into the spectrograph, and a shutter mechanism for controlling exposure times.

To determine exposure times, a photometer should be used to monitor star brightness. In order to avoid subtracting light from the main beam, a small mirror near the échelle can be used to divert part of the undispersed ($\beta \equiv -\alpha$) zeroeth order to a suitable photomultiplier tube and meter.

Grating Ordering Information

The échelle grating shown in Figure 4.3 is one made on a Bausch and Lomb size 20 blank, cut in half. Thus the blank is 65 × 165 × 30 mm, and ruled over an area of 56 × 152 mm ($\ell \times \omega$). For the cross-disperser grating, either this same size or a size 17 blank could be used. The size 17 grating, shown in Figure 4.3, is 110 × 135 × 25 mm, ruled over an area of 102 × 128 mm ($\omega \times \ell$). Note that this ruling is perpendicular to the one normally supplied. The échelle costs $2000, plus an extra $400 for the hole. The size 17 gratings cost $995 each (U.S. prices, as of September 1979).

REFERENCES

J.G. Baker, "A Family of Flat-Field Cameras, Equivalent in Performance to the Schmidt Camera", Proc. of the American Phil. Society, 82, 339-349 (1940).

I.S. Bowen, "The Spectrographic Equipment of the 200-Inch Hale Telescope", Astrophysical Journal, 116, 1-7 (1952).

J.B. Breckinridge, A.K. Pierce and C.P. Stoll, "Thorium Comparison Spectrum", Astrophysical Journal, Supplement Series, 29, 97-112 (1975).

W.M. Burton, "A Compact Astronomical Échelle Spectrograph", Observatory, 97, 132-139 (1977).

C.I. Coleman, "High DQE Image Detectors", International Conference on Image Analysis and Evaluation (Toronto), Paper Th B3 (1976).

F.S. Crawford, Jr., "Waves", Berkeley Physics Course - Volume 3 (3rd edition), McGraw-Hill (1968).

R.H. Cromwell and R.R. Dyvig, "Laboratory Evaluation of Eleven Image Intensifiers", Optical Sciences Centre, University of Arizona, Technical Report 81 (1973).

S.C.B. Gascoigne, "Some Recent Advances in the Optics of Large Telescopes", Quarterly Journal of the Royal Astr. Society, 9, 98-115 (1968).

D.F. Gray, "The Observation and Analysis of Stellar Photospheres", Wiley (1976).

C.F.W. Harmer, "Pupil Imagery in Astronomical Spectrographs", Monthly Notices of the Royal Astr. Society, 167, 311-318 (1974).

ITT, "Magnetic Focus Image Intensifiers for Photographic Applications", Application Note E20, and accompanying product information (revised, no date), Electro-Optical Products Division, ITT (1974).

P. Jacquinot, "The Luminosity of Spectrometers with Primary, Gratings, or Fabry-Perot Etalons", Journal of the Optical Society of America, 44, 761-765 (1954).

Jobin Yvon, "Handbook of Diffraction Gratings Ruled and Holographic", (revised edition), Jobin Yvon (1978).

J. Junkes and E.W. Salpeter, "Spectrum of Thorium from 9400 to 2000 Å", Vatican City: Specola Vaticana (1964).

Kodak, "Kodak Plates and Films for Scientific Photography", (1st edition), publication P-315, Eastman Kodak (1973).

Kodak, "Kodak Special Plates, Type 127-04 and Type 127-05", (now called Type IIIa-F), data release, Eastman Kodak (1976).

Kodak, "Hypersensitizing of Infrared Emulsions by Bathing in Silver Nitrate Solution", publication P7-670, Eastman Kodak (1979).

R.C.M. Learner, "Échelle Grating Spectrographs for the Cassegrain Focus of the AAT", Proc. of the ESO/CERN Conference on Auxiliary Instrumentation for Large Telescopes, 131-140 (1972).

E.H. Linfoot, "Recent Advances in Optics", Oxford (1955).

E.G. Loewen, "Diffraction Gratings for Large Telescopes", Proc. of the ESO/CERN Conference on Auxiliary Instrumentation for Large Telescopes, 193-202 (1972).

E.G. Loewen, "Selection Rules for Diffraction Gratings", Electro-Optical Systems Design, August, 26-27 (1977).

E.G. Loewen, M. Nevière and D. Maystre, "Grating Efficiency Theory as it Applies to Blazed and Holographic Gratings", Applied Optics, 16, 2711-2721 (1977).

Melles Griot, "Optics Guide", Costa Mesa, California: Melles Griot (1975).

Optical Society of America, "Handbook of Optics", W.G. Driscoll and W. Vaughan, editors, McGraw-Hill (1978).

A.M. Schneiderman and D.P. Karo, "How to Build a Speckle Interferometer" in "Imaging Through the Atmosphere", Proc. SPIE, 75 (1976).

D.J. Schroeder, "Design Considerations for Astronomical Échelle Spectrographs", Publ. of the Astr. Society of the Pacific, 82, 1253-1275 (1970).

D.J. Schroeder, "Échelle Spectrographs", Proc. of the ESO/CERN Conference on Auxiliary Instrumentation for Large Telescopes, 119-130 (1972).